

MODELLING AND CONTROL OF THE LLC RESONANT CONVERTER

by

Brian Cheak Shing Cheng

B.Sc., Queen's University, 2010

A THESIS SUBMITTED IN PARTIAL FULFILLMENT OF

THE REQUIREMENT FOR THE DEGREE OF

MASTER OF APPLIED SCIENCE

in

The Faculty of Graduate Studies

(Electrical & Computer Engineering)

THE UNIVERSITY OF BRITISH COLUMBIA

(Vancouver)

December 2012

© Brian Cheak Shing Cheng, 2012

Abstract

To achieve certain objectives and specifications such as output voltage regulation, any power electronics converter must be coupled with a feedback control system. Therefore, a topic of considerable interest is the design and implementation of control systems for the LLC resonant converter. Additionally, with the current trend of smaller, more cost effective and reliable digital signal processors, the implementation of digital feedback control systems has garnered plenty of interest from academia as well as industry.

Therefore, the scope of this thesis is to develop a digital control algorithm for the LLC resonant converter. For output voltage regulation, the LLC resonant converter varies its switching frequency to manipulate the voltage gain observed at the output. Thus, the plant of the control system is represented by the small signal control-to-output transfer function, and is given by $P(s) = \frac{V_o}{f}$.

The difficulty in designing compensators for the LLC resonant converter is the lack of known transfer functions which describe the dynamics of the control-to-output transfer function. Thus, the main contribution of this thesis is a novel derivation of the small signal control-to-output transfer function. The derivation model proposes that the inclusion of the third and fifth harmonic frequencies, in addition to the fundamental frequency, is required to fully capture the dynamics of the LLC resonant converter. Additionally, the effect of higher order sideband frequencies is also considered, and included in the model.

In this thesis, a detailed analysis of the control-to-output transfer function is presented, and based on the results, a digital compensator was implemented in MATLAB[®]. The compensator's functionality was then verified in simulation.

A comparison of the derivation model and the prototype model (based on bench measurements) showed that the derivation model is a good approximation of the true system dynamics. It was therefore concluded that both the bench measurement model and the derivation model could be used to design a z-domain digital compensator for a digital negative feedback control system. By using the derivation model, the main advantages are reduced computational power and the requirement for a physical prototype model is diminished.

Table of Contents

Abstract	ii
Table of Contents	iii
List of Tables	vi
List of Figures	vii
List of Symbols	ix
List of Abbreviations	xi
List of SI Units and Prefixes	xii
Acknowledgments	xiii
Dedication	xiv
1 Introduction	1
1.1 Background	1
1.2 Motivation	2
2 LLC Resonant Converter	3
2.1 H-bridge Inverter	6
2.1.1 Zero Voltage Switching	7
2.2 Resonant Tank	8
2.2.1 Resonant Frequencies ω_{r1}, ω_{r2}	9
2.2.2 High Frequency Isolation Transformer	9
2.3 Rectifier	10
2.3.1 Synchronous Rectification	11
2.4 Theory of Operation	14
2.4.1 Region 1	15
2.4.2 Region 2	15
3 Control of LLC Resonant Converter	18
3.0.3 Variable Frequency Control	18
3.0.4 Pulse Width Modulation	19
3.1 Digital Control	19
3.1.1 Effects of Sampling Frequency	20

3.1.2	Design of Digital Control Systems	20
3.1.3	2-Pole-2-Zero Compensator	21
3.2	Compensator Design	22
3.2.1	Root Locus	22
3.2.2	Bode Diagram	22
3.3	Stability	23
3.3.1	Bode Diagram	23
3.3.2	Nyquist Plot	23
4	Implementation and Verification	25
4.1	Design Methodology	25
4.1.1	Overview	25
4.1.2	Bench Test Results	26
4.1.3	Compensator Design Results	27
4.1.4	Verification in PSIM [®]	30
4.2	Texas Instruments [®] DSP	34
5	Derivation of Control-to-Output Transfer Function	36
5.1	Overview	36
5.2	Transfer Function Derivation	36
5.2.1	Frequency Modulation	37
5.2.2	Square Wave Approximation	38
5.2.3	Bessel Functions of the First Kind	39
5.2.4	Amplitude Modulation	41
5.2.5	Results of Frequency and Amplitude Modulation	45
5.2.6	Isolation Transformer and Rectification Stage	47
5.2.7	Results of Analysis of the Derivation Model	47
5.2.8	Phase Response of Control-to-Output Transfer Function	48
5.3	Verification of Derivation Model in PSIM [®]	50
6	Conclusions and Future Work	54
6.1	Summary	54
6.2	Future Work	55
	References	56
	Appendices	59
	Appendix A: Observation of Stability in Continuous and Discrete-time domains	59
	A1: Continuous-time domain	59

A2: Discrete-time domain	60
Appendix B: PSIM [®] simulation schematic	61
Appendix C: MATLAB [®] derivation model code	62

List of Tables

1	Results of prototype model	32
2	Results of derivation model	53

List of Figures

1	A direct link between DC source(s) and load(s)	1
2	Resonant tank circuits of resonant converter topologies	3
3	LCC resonant tank circuit schematic	4
4	Comparison of LCC and LLC DC gain characteristic with varying Q-factors	5
5	LLC resonant converter circuit schematic	5
6	H-bridge inverter circuit schematic	7
7	Resonant tank circuit schematic	8
8	Rectifier circuit modelled as R_{ac}	10
9	SR phase delay	12
10	Synchronous rectification PSIM® model	13
11	Regions 1, 2, and 3	14
12	Operation of LLC resonant converter in region 1	16
13	Operation of LLC resonant converter in region 2	17
14	Block diagram of negative feedback loop	18
15	Block diagram of digital negative feedback loop	19
16	2 pole 2 zero DSP implementation	22
17	Bench test result of DC gain characteristic for Region 1	26
18	Plot of relative frequency response of prototype model under different loading conditions	27
19	Prototype model frequency response data in MATLAB® SISOTOOL GUI environment	28
20	Open-loop Bode plot of prototype frequency response data	29
21	MATLAB® step response of closed-loop system using prototype model	30
22	PSIM® circuit schematic of LLC resonant converter	31
23	PSIM® controller schematic of LLC resonant converter	31
24	Error voltage of prototype model	31
25	Output voltage ripple of prototype model	32
26	PSIM® closed-loop response to step load change using prototype model	33
27	Voltage loop flow diagram for DSP implementation	35
28	Analysis road map	37
29	Tank filter circuit schematic with equivalent resistance R_{ac}	43
30	Comparison of the significance between fundamental, third and fifth harmonics	46
31	Comparison of the fundamental component, with and without sideband frequencies .	46
32	Comparison of prototype frequency response data and derivation model (magnitude)	48
33	Comparison of derivation model and curve fit model (magnitude)	49
34	Comparison of prototype frequency response data and curve fit model (phase)	50
35	MATLAB® step response of closed-loop system using derivation model	50

36	Error voltage of derivation model	51
37	Output voltage ripple of derivation model	51
38	PSIM® closed-loop response to step load change using prototype model	52
A-1	Unit circle in the z-domain	60
B-1	PSIM® closed loop circuit schematic of LLC resonant converter	61
B-2	PSIM® open loop circuit schematic of LLC resonant converter	61

List of Symbols

a_n	n^{th} coefficient of 2P2Z transfer function denominator
b_n	n^{th} coefficient of 2P2Z transfer function numerator
C_o	output capacitor
C_p	parallel resonant capacitor
C_r	series resonant capacitor
E	energy of carrier and sideband frequency signals
$e[k - n]$	n^{th} previous error term
f_s	switching frequency
f_{sample}	sampling frequency
f_{max}	maximum bandwidth frequency
$J_n(\beta)$	Bessel function of the first kind
K_{VCO}	VCO gain constant
L_M	magnetizing inductor
L_r	series resonant inductor
N	transformer turns ratio
$N_{primary}$	number of turns on primary side of transformer
$N_{secondary}$	number of turns on secondary side of transformer
p_i	i^{th} pole
P_{sw}	power loss of semiconductor switch device
Q	ratio between the characteristic impedance and the output load
r	reference input
R_{ac}	equivalent AC resistance
R_c	output capacitor equivalent series resistance
R_o	output resistance
R_r	series resistance
T	sampling time
T_{off}	semiconductor switch device turn off time
T_{on}	semiconductor switch device turn on time
$u[k - n]$	n^{th} previous term of compensator output
V_{ctrl}	control voltage
V_{ds}	drain-source voltage
V_g	input voltage
V_o	output voltage
V_p	peak voltage

$V_{s,1}$	fundamental component voltage expression
$V_{s,3}$	third harmonic voltage expression
$V_{s,5}$	fifth harmonic voltage expression
z_i	i^{th} zero
β	modulation index
ϵ	amplitude of small signal perturbation
$\Gamma(x)$	gamma function
ω_c	angular carrier frequency
ω_m	angular modulation frequency
ω_r	angular resonant frequency
$\hat{\omega}$	voltage controlled oscillator free-running angular frequency
$=$	equals
\neq	not equal to
\approx	approximately equal to
\pm	plus and minus

List of Abbreviations

2P2Z	2-pole-2-zero
AC	alternating current
ADC	analog-to-digital converter
AM	amplitude modulation
DAC	digital-to-analog converter
CLA	Control Law Accelerator TM
CPU	central processing unit
DC	direct current
DSP	digital signal processor
EMI	electromagnetic interference
FM	frequency modulation
GUI	graphical user interface
LCC	inductor-capacitor-capacitor
LLC	inductor-inductor-capacitor
LPF	low pass filter
MOSFET	metal oxide semiconductor field effect transistor
P	proportional control
PI	proportional, integral control
PID	proportional, integral, derivative control
PWM	pulse-width modulation
RHPZ	right hand plane zero
SISO	single input single output
SMPS	switched-mode power supply
SR	synchronous rectifier
UPS	uninterruptible power supply
VCO	voltage-controlled oscillator
ZVS	zero-voltage switching
ZCS	zero-current switching
ZOH	zero-order hold

List of SI Units and Prefixes

A	amperes
dB	decibel
Hz	hertz
s	seconds
V	volts
°	degrees

p	pico(10^{-12})
n	nano (10^{-9})
μ	micro (10^{-6})
m	milli (10^{-3})
k	kilo (10^3)
M	Mega (10^6)
G	Giga (10^9)
T	Tera (10^{12})

Acknowledgments

I would first like to express my sincere and utmost gratitude to my research supervisor, Dr. William Dunford, for his patience and guidance throughout my studies at UBC. His support and mentorship in both my academic and professional endeavors has been invaluable, and I am indebted to him for his help over the past two years.

Secondly, I would like to thank my friends and colleagues at the UBC Electric Power and Energy Systems Group. My time at UBC has been much more memorable because of the people I have met here. In particular, I'd like to thank Rahul Baliga, Justin Wang, and William Wang for the many technical and non-technical discussions that have been had. Additionally, I would like to thank my former classmates and friends Colin Clark and Kyle Ingraham for their technical advice and friendship.

I would also like to thank the Natural Sciences and Engineering Research Council of Canada (NSERC) and Alpha Technologies Ltd. for their generous financial support of this research project. I must give my extended gratitude to Mr. Victor Goncalves for giving me the opportunity to complete my internship at Alpha Technologies Ltd., as well as the many people I was fortunate enough to collaborate with at Alpha Technologies Ltd. The technical expertise I received over the course of this work was indispensable. Additionally, I would also like to thank Mr. Brian Bella of the Faculty of Graduate Studies at UBC for his assistance with the application to the Industrial Postgraduate Scholarship program.

Last but not least, I must thank my family for their unconditional support throughout the years. Growing up, they have been my source of inspiration, and have provided me with exemplary examples of the person I one day hope to become. To each of them, I owe my deepest gratitude. I would like to take this opportunity to individually thank each of these people who have made it possible for me to get to where I am today. My grandmother; my parents Tom and Daisy, my uncles and aunts Patrick and Janet; Millie and Gilbert, Cora and Joe; and Juno and Alex. A special 'thank you' also needs to extended to my cousins Jeffrey, Steven, Gibson, Jackie and Megan, who have all become like my own brothers and sisters.

Finally, I would like to acknowledge and thank my grandfather, whose memory remains strong with us to this very day.

Dedicated to my parents

1 Introduction

1.1 Background

Switched-mode power supplies (SMPS) are now found in many different industrial applications and their function can vary from high power electric vehicles to low power biomedical devices and equipment. There is particular interest in applying SMPS to medium and high power applications for uninterruptible power supplies (UPS) designed for telecommunications-grade applications.

The next generation of SMPS aim to achieve high efficiency, high reliability, high power density, as well as low cost. As an example, in renewable energy applications, due to constraints in cost and the physical limitations of energy storage, the benefits of a well designed SMPS are immediate.

The application of DC-DC converters has recently become an important area of SMPS design as the emergence of distributed generation and battery-based systems continues to grow. Additionally, as the number of DC loads increases [1], using local DC power sources becomes more of a sensible solution, and further encourages the development of DC-DC conversion technology.

For some applications, DC-DC converters are particularly useful, as it provides a direct interface between energy storage elements, which are typically DC voltage sources, and DC loads. By reducing the number of intermediate energy conversion processes, the overall efficiency of the system can be increased, while also potentially minimizing the cost of the system. To meet safety and protection requirements, DC-DC converters can also be implemented with galvanic isolation between the input source and output load.

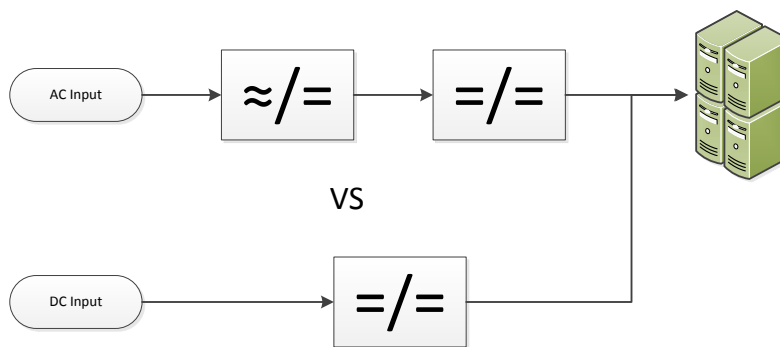


Figure 1: A direct link between DC source(s) and load(s)

A particular form of DC-DC converter is the resonant converter. In literature, resonant converters have been thoroughly studied and it has been shown that they can offer many benefits in performance, size, and cost [2]. For example, resonant converters are able to achieve low switching losses through the use of soft-switching techniques, and are able to be operated at greater switching

frequencies than other comparable converters.

The ability to operate at higher switching frequencies has the superior advantage of increasing efficiency, as well as decreasing the size of the discrete components, notably inductors and capacitors, within the hardware. This is in comparison to pulse-width modulation (PWM) converters, where the turn-on and turn-off losses of the switching devices at high switching frequencies can be high enough to prohibit operation of the converter, even when soft-switching techniques are used [3].

Moreover, PWM converters utilizing high switching frequency operation can cause disturbances such as electromagnetic interference (EMI) and suffer from the effects of parasitic impedances. However, under proper design, it is possible for resonant converters to utilize the leakage inductances of the circuit as part of the resonant tank circuit. It was also found that certain resonant converters are able to operate with low EMI [4]. Because of these advantages, resonant converters with switching frequencies in the range of MHz are conceivable [2][5].

Some typical resonant topologies include the series resonant, parallel resonant, and the series-parallel resonant converters.

1.2 Motivation

Because of the demand for resonant conversion, methods on how to design effective feedback control systems for resonant converters becomes a topic of considerable interest. To make a converter valuable for practical system applications, and to achieve specifications such as output voltage regulation, it is necessary to adopt some form of feedback control. Furthermore, with the advancements in digital signal processors, digital control techniques have become a feasible option. The application of digital controllers has allowed for more flexible designs when compared to analog controllers, and allows for much greater reliability and system integration.

Consequently, this thesis will be centered around designing and implementing a digital control system for a resonant power electronics converter topology to be used in a medium power application. Chapter 2 will discuss in detail a resonant converter topology, followed by discussion on implementing a digitally controlled negative feedback control loop for output voltage regulation in Chapters 3 and 4. Lastly, a novel mathematical model of the small signal control-to-output transfer function is presented in Chapter 5.

2 LLC Resonant Converter

Resonant power converters contain L-C networks, or resonant tanks, whose voltage and current waveforms vary sinusoidally during one or more subintervals of each switching period [6]. Three well-known resonant topologies include the series resonant, parallel resonant, and series-parallel resonant. Although there are peculiar differences in each of these topologies, the essential operation is the same: a square pulse of voltage or current is generated, and applied to the resonant tank circuit. Energy circulating within the resonant tank will then either be fully supplied to the output load, or be dissipated within the tank circuit [2].

As documented in [7], the series and parallel resonant topologies shown in Figure 2 have several limiting factors which make them the non-ideal choice for practical applications. For the series resonant converter topology, light load operation requires a very wide range of switching frequencies in order to retain output voltage regulation. It was also observed that for high input voltage conditions, the series resonant converter suffers from high conduction losses, and the switching network transistors experience high turn-off current.

Compared to the series resonant converter, the parallel resonant converter topology does not require a wide range of switching frequencies to maintain output voltage regulation. However, at high input voltage conditions, the parallel resonant converter shows worse conduction losses, and higher turn-off currents.

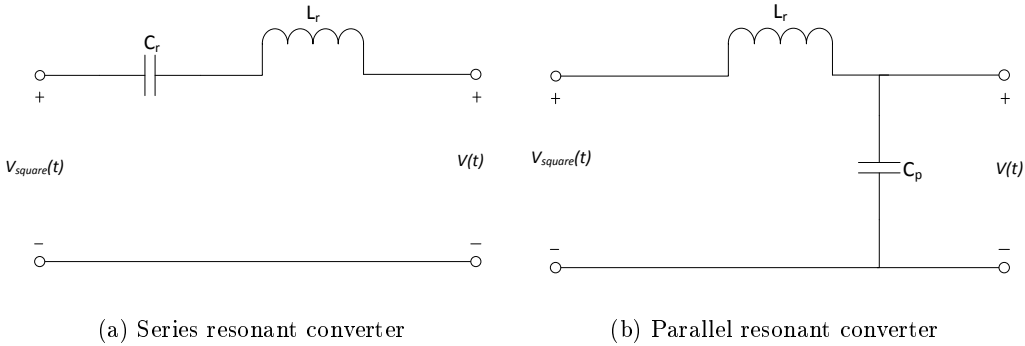


Figure 2: Resonant tank circuits of resonant converter topologies

One possible solution to overcome the deficiencies found in the above two converters is the series-parallel or LCC (inductor-capacitor-capacitor) converter shown in Figure 3. Since it is known that the operation around the resonant frequency has the greatest efficiency, it is desired to operate the converter around this operating point [7].

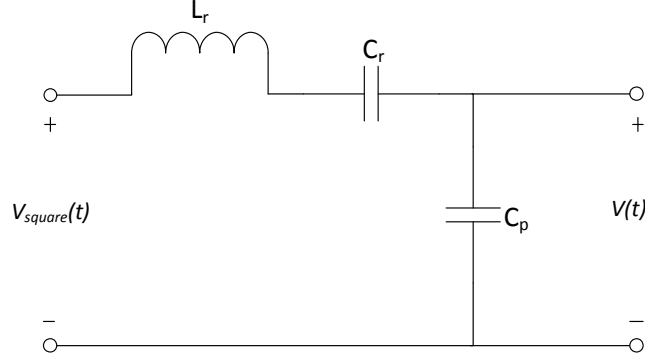


Figure 3: LCC resonant tank circuit schematic

Figure 4a plots the DC gain characteristic of the LCC resonant converter with different values of the variable Q , and it can be seen in Figure 4a that more than one resonant frequency exists, depending on value of Q . Q is defined as the ratio between the characteristic impedance and the output load and can be given by Equation 1 [8].

$$Q = \frac{\sqrt{\frac{L_r}{C_r}}}{R} \quad (1)$$

where R is defined as the value of the output load resistance.

Furthermore, from the DC gain characteristic of Figure 4, it is understood that the segments of the DC gain characteristic with a positive gradient are regions intended for zero-current switching (ZCS) operation [7]. Given that the designed converter is to use metal-oxide field effect transistors (MOSFET) as the semiconductor switching device, the desired region of operation should therefore be on the negative gradient, a region intended for zero-voltage switching (ZVS) operation [7]. This is because the preferred soft-switching mechanism of MOSFET devices is ZVS. As outlined in [6], ZVS mitigates the switching loss otherwise caused by diode recovery charge and semiconductor capacitance often found in MOSFET switching devices.

Since it is known that operation on the negative gradient of the DC gain characteristic is desired, the characteristics of this operating region should be observed. As an example, it can be seen in Figure 4a that to achieve a gain value of 1.0 for increasing values of Q , the range of the ratio of the switching frequency to the resonant frequency $\frac{f_s}{f_r}$ varies from 0.7 to 1.2. Therefore, it can be noted that a fairly large range of switching frequencies is required to maintain a gain value of 1.0 when the output load is changing.

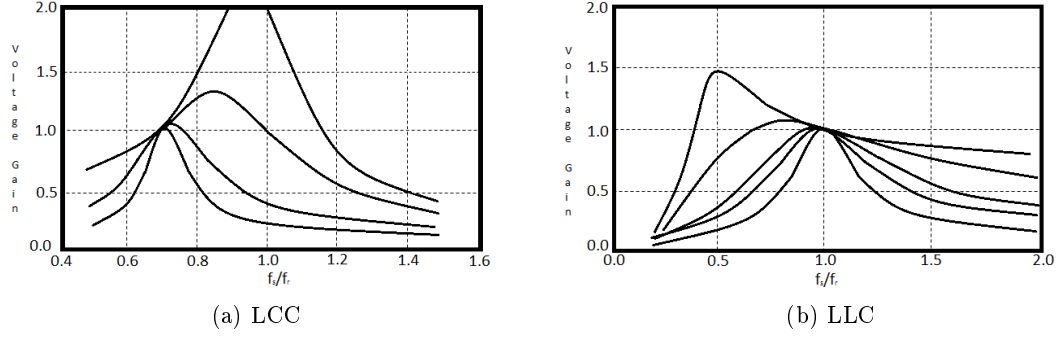


Figure 4: Comparison of LCC and LLC DC gain characteristic with varying Q-factors

With this understanding of the LCC converter characteristics, the LLC (inductor-inductor-capacitor) resonant converter shown in Figure 5 becomes a potential solution. Essentially the dual of the LCC converter, the DC gain characteristics of Figure 4a are reversed in the LLC resonant converter and are shown in Figure 4b.

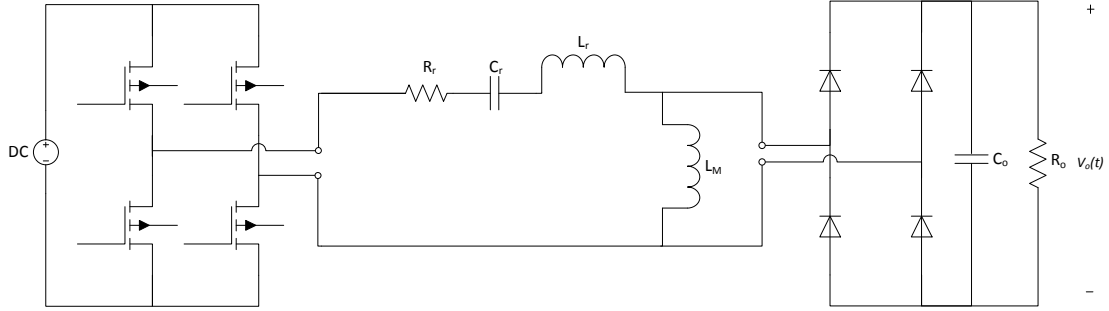


Figure 5: LLC resonant converter circuit schematic

From Figure 4b, it can be seen that the operation at around the resonant frequency, the operation is in a region such that the DC gain characteristic has a negative gradient and therefore, ZVS capabilities can be achieved in this region. Furthermore, by observing the DC characteristic of Figure 4b, and what was noted about the switching frequency range of the LCC, it can be seen that in the LLC resonant converter, the gain value of 1.0 can be achieved for all loading conditions within a very narrow range of switching frequencies.

An additional benefit of the LLC DC gain characteristic is that the resonant frequency of Figure 4b has now shifted to a higher switching frequency in comparison to the equivalent ZVS region resonant frequency of Figure 4a, and thus the potential for improvements in efficiency and

power density are greatly improved.

Some other advantages of the LLC resonant converter over other resonant topologies is its ability to maintain ZVS characteristics under light load conditions, and low electromagnetic interference (EMI) [4].

Since it has now been determined that the LLC resonant converter has many favorable features for DC-DC conversion applications, Sections 2.1 - 2.4 will discuss each stage of the LLC resonant converter, as well as the theory of operation.

2.1 H-bridge Inverter

The first stage of the LLC resonant circuit is the H-bridge inverter. It is composed of four triode-mode MOSFET transistors which are used to invert the input DC voltage to an AC sinusoidal waveform. The use of MOSFET switches are preferred since they have high input impedance and can operate at very fast switching speeds [9]. And as previously discussed, for efficiency purposes, the LLC resonant converter utilizes ZVS to eliminate the switching losses of the MOSFETs. Finally, the frequency at which the switches are turned on and off will determine the frequency to be applied to the resonant tank.

To be more precise, the H-bridge generates a square wave with frequency f_s equal to the frequency of the MOSFET switching. This quasi-square wave is established by switching on diagonally placed switches at the same time to generate the high and low values of the square-wave waveform.

It can also be noted that to prevent a shoot through condition, a small dead band time can be included between the turn-on and turn-off times of the diagonal switches.

Finally, the quasi-square wave output can be mathematically characterized by Equation 2 and the basic circuit configuration of the H-bridge inverter can be given by Figure 6.

$$v_{square}(t) = \sum_{n=1,3,5,\dots}^{\infty} \frac{4V_g}{n\pi} \sin(n2\pi f_c t) \quad (2)$$

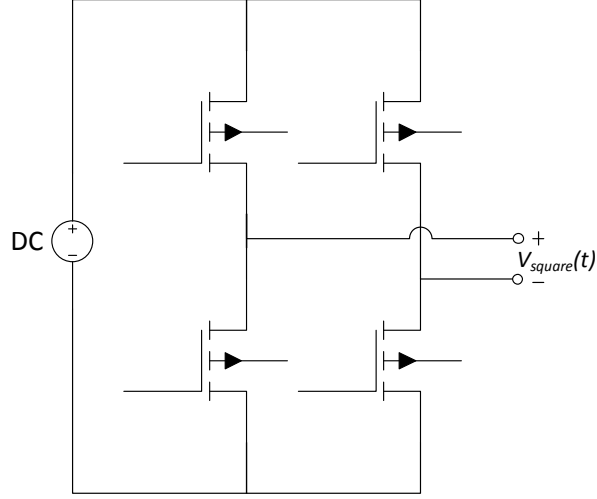


Figure 6: H-bridge inverter circuit schematic

2.1.1 Zero Voltage Switching

Zero voltage switching (ZVS) is the preferred soft-switching mechanism for MOSFET devices, as it mitigates the switching loss caused by diode recovery charge and semiconductor output capacitance [6]. In [10], switching loss is defined as the simultaneous overlap of voltage and current in power MOSFET switches.

It is shown in [10] that by allowing the drain-to-source voltage V_{ds} to reach zero before the switch turns on, the switching power loss is made to be zero. However, when there is overlap between V_{ds} and the current i_{ds} , a non-zero loss can be observed. To allow V_{ds} to reach zero, the internal capacitance of the MOSFET must be discharged by reversing the direction of the current flow through the MOSFET.

In general, ZVS occurs when the switching network is presented with an inductive load, and hence, the switch voltage zero crossings lead the zero crossings of the switch current [6]. In the case of the LLC resonant converter, ZVS operation of the H-bridge inverter switching devices is achieved and maintained by the presence of the magnetizing inductance [3][11].

An additional benefit of ZVS is the reduction of electromagnetic interference (EMI) typically associated with switching device capacitances [6].

2.2 Resonant Tank

The resonant tank circuit is the chief constituent of the LLC resonant converter, and is comprised of series resonant inductor L_r , series resonant capacitor C_r , and a parallel resonant inductor L_M . There are numerous possible configurations in which the tank components can be arranged, but the most frequently used arrangement found in literature is the connection of L_r and C_r in series and inductor L_M in parallel to the load. This arrangement is identical to the series resonant topology with the addition of inductor L_M . For a more complete model of the resonant tank, a series resistor can also be included.

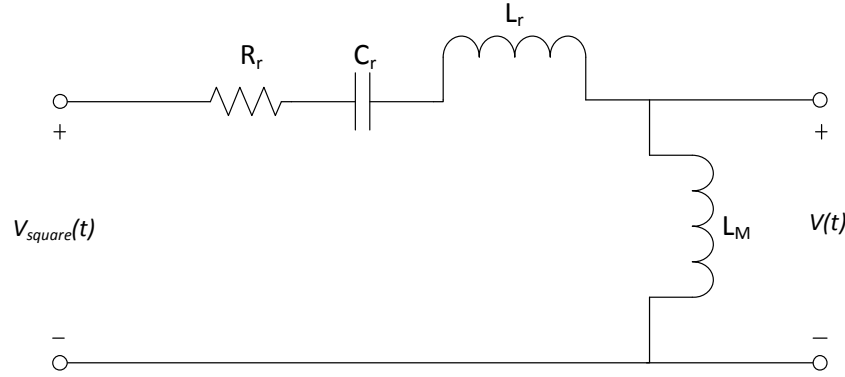


Figure 7: Resonant tank circuit schematic

The no-load transfer function of the LLC resonant tank circuit shown Figure 7 is given by Equation 3

$$H(s) = \frac{s^2(L_M C_r)}{s^2 C_r (L_M + L_r) + s C_r R_r + 1} \quad (3)$$

Well-known relationships between impedance and frequency are given by Equation 4.

$$Z_L = j\omega L \quad (4)$$

$$Z_C = \frac{1}{j\omega C}$$

From these fundamental equations, it is shown that the impedance of the resonant tank can be tuned according to the frequency applied to the tank circuit. It can then be said that by varying the impedance of the resonant tank, that the voltage gain seen at the output will differ, depending

on the frequency applied to the resonant tank. It is then concluded that this voltage gain will determine the attainable output voltage value, and thus is the method in which output voltage regulation can be achieved with the LLC resonant converter.

2.2.1 Resonant Frequencies ω_{r1}, ω_{r2}

From the values of L_r , C_r , and L_M , two important operating conditions can be identified: ω_{r1} and ω_{r2} . These operating points are defined as the resonant frequencies, and are defined by the applied loading condition. From Figure 7, it can be seen that at the no-load condition, the inductance L_M is seen by the tank circuit as a passive load and thus, the resonant frequency can be given by Equation 5.

$$\omega_{r2} = \frac{1}{\sqrt{(L_r + L_M)C_r}} \quad (5)$$

In the case where a nominal load is applied, the load seen by the resonant tank is effectively the large output capacitance C_o in parallel with inductance L_M . Thus, the inductor L_M is bypassed by the effective AC short circuit and the resonant frequency can be given by Equation 6.

$$\omega_{r1} = \frac{1}{\sqrt{L_r C_r}} \quad (6)$$

In this thesis, operation is focused around the resonant frequency given by Equation 6, as this operating point allows for greater efficiency, and allows for regulation using only a narrow range of switching frequencies.

2.2.2 High Frequency Isolation Transformer

Following the resonant tank circuit is a high frequency isolation transformer that can be used to either buck or boost the sinusoidal voltage to the secondary side of the converter. The transformer also serves the dual purpose of providing galvanic isolation, such that no direct current flows between the input and output.

A rather remarkable feature of the transformer is that the magnetizing and leakage inductances can be used as part of the tank circuit. For instance, the magnetizing inductance of the transformer can be used as or part of the parallel resonant inductance L_M , therefore potentially reducing the number of additional discrete components required. Similarly, the leakage inductance can be made a part of the series inductor L_r , depending on the design of the transformer parameters. This so-called integrated magnetic can therefore be designed to serve the purpose of potentially increasing the converter's power density.

The transformer ratio between the primary and secondary sides is given by the transformer turns ratio and shown by Equation 7.

$$N = \frac{N_{secondary}}{N_{primary}} \quad (7)$$

2.3 Rectifier

The last stage of the LLC resonant converter is the full bridge rectifier with capacitor output filter, which transforms the AC waveform to DC output. Similar to what was found in [6] and [12], the full bridge rectifier with capacitor filter is modelled as resistor R_{ac} . The relationship between R_{ac} and the output load is given by

$$R_{ac} = \frac{V_I}{I_{ac}} = \frac{8V_o}{\pi^2 I_o} = \frac{8}{\pi^2} R_o \quad (8)$$

R_{ac} can then be reflected onto the primary side by multiplying Equation 8 by the transformer turns ratio given by Equation 7.

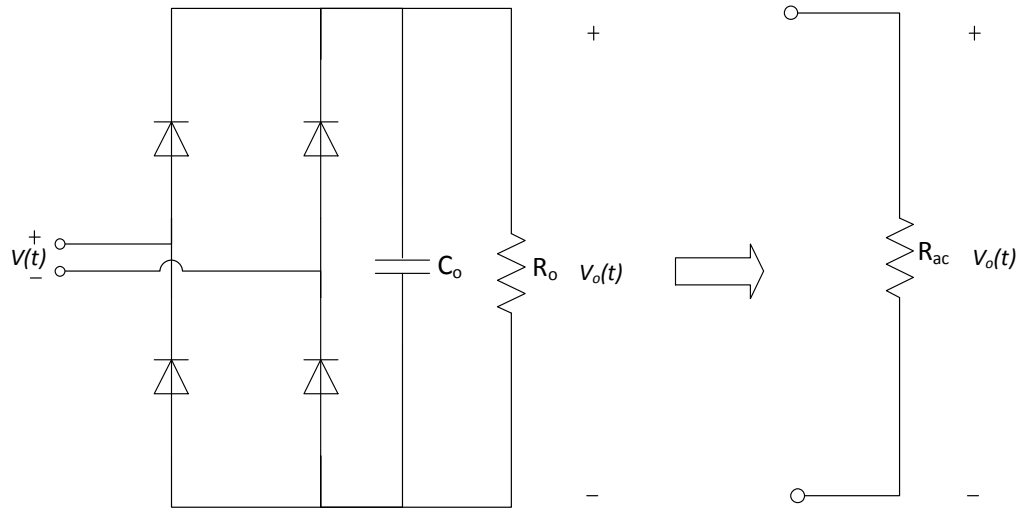


Figure 8: Rectifier circuit modelled as R_{ac}

From [6], the final DC value of the output voltage and the output voltage ripple can also be determined by the following relationships.

$$V_{o,dc} = V_p \left(1 - \frac{1}{2f_s C_o R_o}\right) \quad (9)$$

For the case of an ideal full bridge rectifier that has negligible ripple, the switching frequency f_s and output capacitance C_o are large such that the DC output voltage can be approximated by

Equation 10.

$$V_{o,dc} \approx V_p \quad (10)$$

where V_p is the peak value of the AC input voltage, $V(t)$.

2.3.1 Synchronous Rectification

To further increase the efficiency of the LLC resonant converter, a synchronous rectification (SR) network can be implemented in lieu of the full bridge diode rectifier. In a synchronous rectifier, the diodes are replaced with MOSFET devices, and when current flow is detected on the secondary side, the MOSFETs are turned on to allow current flow to the load.

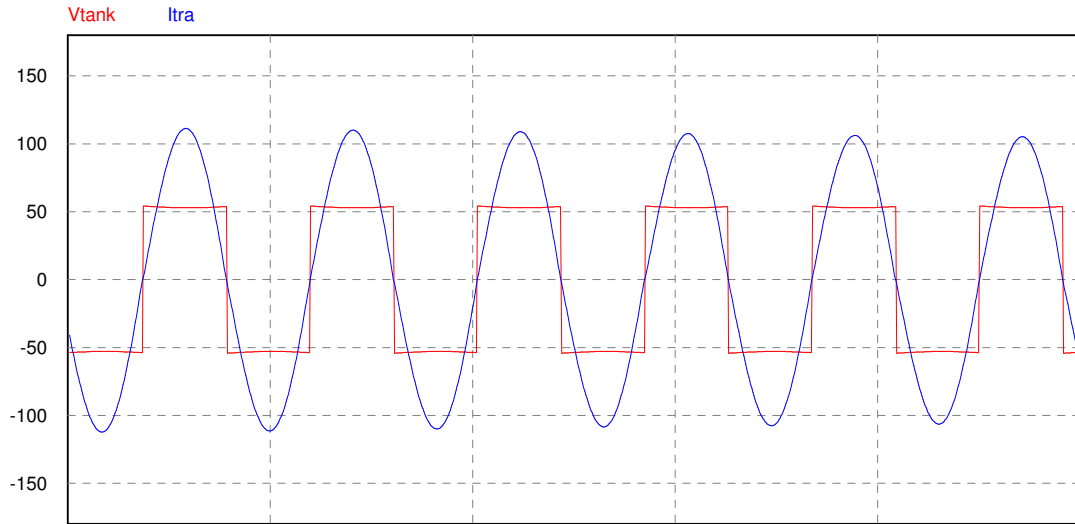
This is a much more efficient strategy in comparison to the diode rectifier, as the voltage drop across the diode is eliminated. Additionally, unlike diodes, which are only able to provide unidirectional flow of power, a SR network makes bidirectional power flow between the input and output feasible.

The disadvantage of implementing SR with the LLC resonant converter is the increased complexity. Computer simulations of Figure B-1 found in Appendix B show the presence of a phase delay between the voltage and current when the switching frequency is away from the resonant frequency. The results of the simulation are shown in Figure 9.

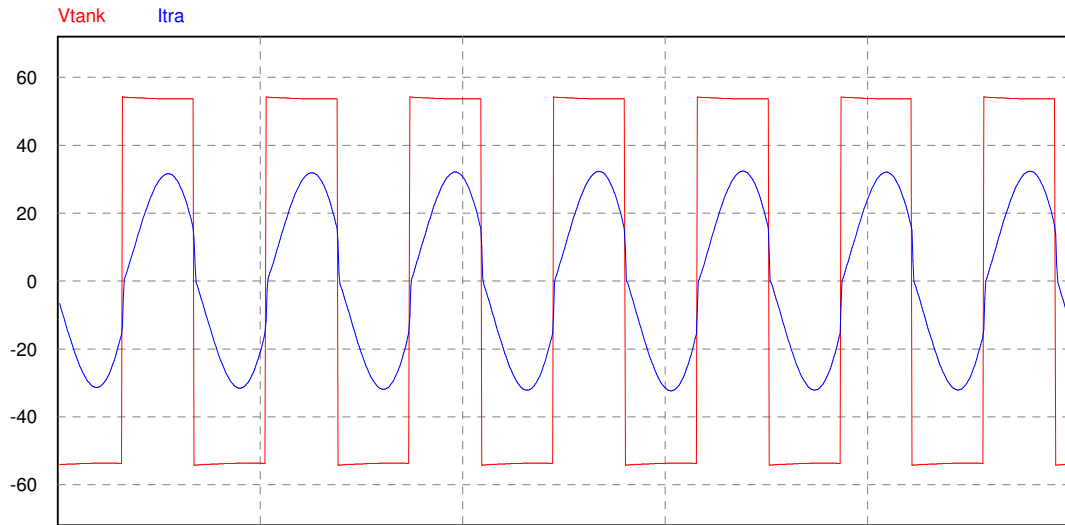
Because of this, it is difficult to determine the timing of the SR turn-on and turn-off. Usually, additional detection circuitry is required on the secondary side to determine when there is current flow through the rectifier, and to determine the control signal to the gates of the SR MOSFETs. Furthermore, since MOSFETs do not have the ability for automatic reverse current blocking, the timing of the turn-off is also important, such that shoot through conditions are avoided.

Some literature has been produced on the control of the SR gate drive signals in [13][14][15]. It is known that the critical event for triggering the SR gate drive signal is the detection of current in the secondary side. It was outlined in [15], that there are two main methods in which this can be accomplished. The first is to directly sense the current using a current transformer. Although this may be the simplest method of detection, the use of a current transformer introduces limitations of the power density as well as the maximum achievable switching frequency. Additionally, the increased series inductance is detrimental to current commutation in the synchronous rectification switch network [15].

Another possible method is to detect the drain-source voltage, V_{ds} of the synchronous rectifier switches. The sensed value of V_{ds} is then processed by control circuits to determine the turn-on and turn-off time of the SRs. This approach can be relatively easily verified in simulation, but the difficulty of this method is determining a method in which V_{ds} can be accurately measured. Because there exists a package inductance from the MOSFETs in the SR, the measured value of



(a) Voltage and current waveforms in phase when $f_s = f_{r1}$



(b) Voltage and current waveforms out of phase when $f_s \neq f_{r1}$

Figure 9: SR phase delay

V_{ds} becomes highly deviated if the package inductance is not properly considered. If the physically sensed value is far deviated from the true value of V_{ds} , a false trigger of the SR circuits may occur, and the potential for shoot through condition increases.

Some literature proposed by [13][14], have shown a number of methods to improve the accuracy of sensing V_{ds} . This is at the expense of circuit complexity, as several additional compensating components are required.

A computer simulation using a current-sensing method has been proposed and is shown in Figure 10.

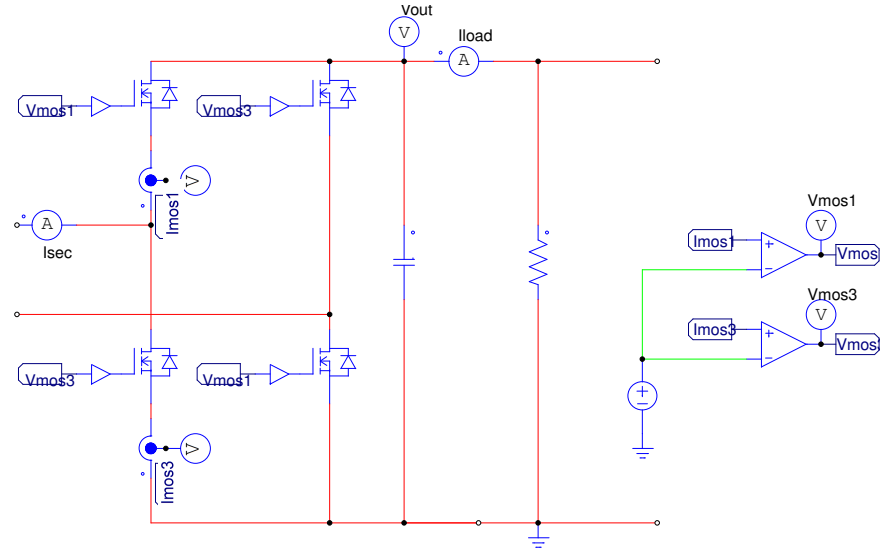


Figure 10: Synchronous rectification PSIM[®] model

2.4 Theory of Operation

The fundamental operation of the LLC resonant converter is based on applying a voltage with frequency f_s to the resonant tank to vary the impedance of the tank circuit, thus controlling the achievable gain seen at the output. From Figure 11, it can be seen that as the switching frequency is increased, the output gain is decreasing. This implies that as the switching frequency is increased, the impedance of the resonant tank is increased, and therefore, a larger voltage drop is observed across the resonant tank circuit components, and less voltage is transferred to the load. The reverse is true as well, such that as the switching frequency decreases, the DC gain increases, implying that the voltage drop across the tank circuit has decreased, and the output voltage gain can be increased.

In the following sections, the operation of the LLC resonant converter is more closely considered, and a single switching interval is analyzed.

There are three main regions of operation, commonly described as Region 1, 2, and 3. Operation in Region 1, 2, and 3 is determined by the location of the operating point on the DC gain curve shown in Figure 11. Region 1 and 2 are located on the negative gradient of the DC gain curve, and Region 3 is located on the positive gradient. Region 1 is the set of switching frequencies greater than the resonant frequency, while Region 2 is the set of switching frequencies below the resonant frequency.

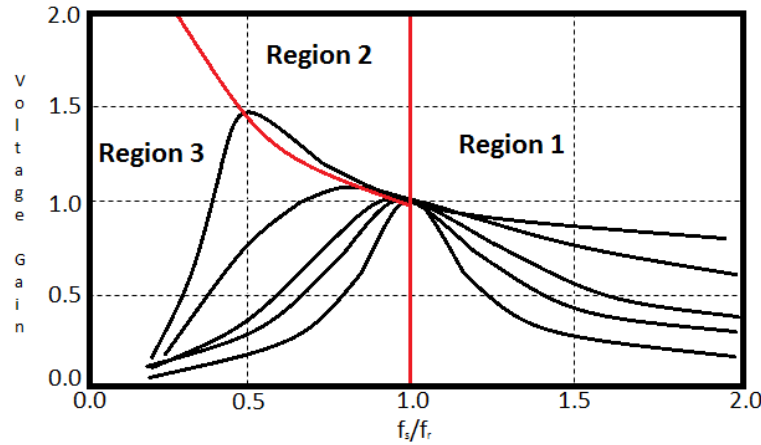


Figure 11: Regions 1, 2, and 3

Depending on the design specifications and requirements that are desired, operation in any of these regions is possible. As it is preferred to switch the MOSFET devices under ZVS conditions, the focus will be on operation in Regions 1 and 2, which is graphically shown in Figure 11 as the negative gradients of the DC gain curves.

2.4.1 Region 1

In Region 1, the magnetizing inductance L_M from the transformer does not resonate with the other tank circuit components, and is viewed as a passive load by the resonating series inductor and series capacitor. Because there is always this passive load, it is possible for the LLC resonant converter to operate at no load without having to force the switching frequency to very high levels. The passive load also ensures ZVS is achieved for all loading conditions [7]. Region 1 operates at the resonant frequency given by Equation 6.

2.4.2 Region 2

In Region 2, there are two distinct operating modes. In the first time sub-interval, the series inductor and series capacitor resonate together while the magnetizing inductance is clamped to the output voltage, and has operation similar to that of Region 1. Therefore, the resonance only occurs between L_r and C_r . The current in the resonant tank I_r then begins to increase and continues to increase until the magnetizing current I_M and I_r are the same. When the two currents are equal, L_M starts to resonate with L_r and C_r , and the second sub-interval begins. Since L_M is now also resonating with the L_r and C_r , the resonant frequency is given by Equation 5.

In Region 2, since multiple resonant frequencies are observed over one switching period, the LLC resonant converter is considered to be a multi-resonant converter. Figure 13 shows the plots of the LLC resonant converter operating in Region 2. Operation in the second sub-interval begins during the time interval in which the output current is equal to zero.

Figures 12 and 13 show the plots of the gate-source drive signal V_{gs} , the resonant current I_r , the magnetizing current I_{LM} , the capacitor voltage V_{Cr} and the output current I_o . Figure B-2 in Appendix B shows the labelled circuit schematic used to obtain the plots of Figures 12 and 13.

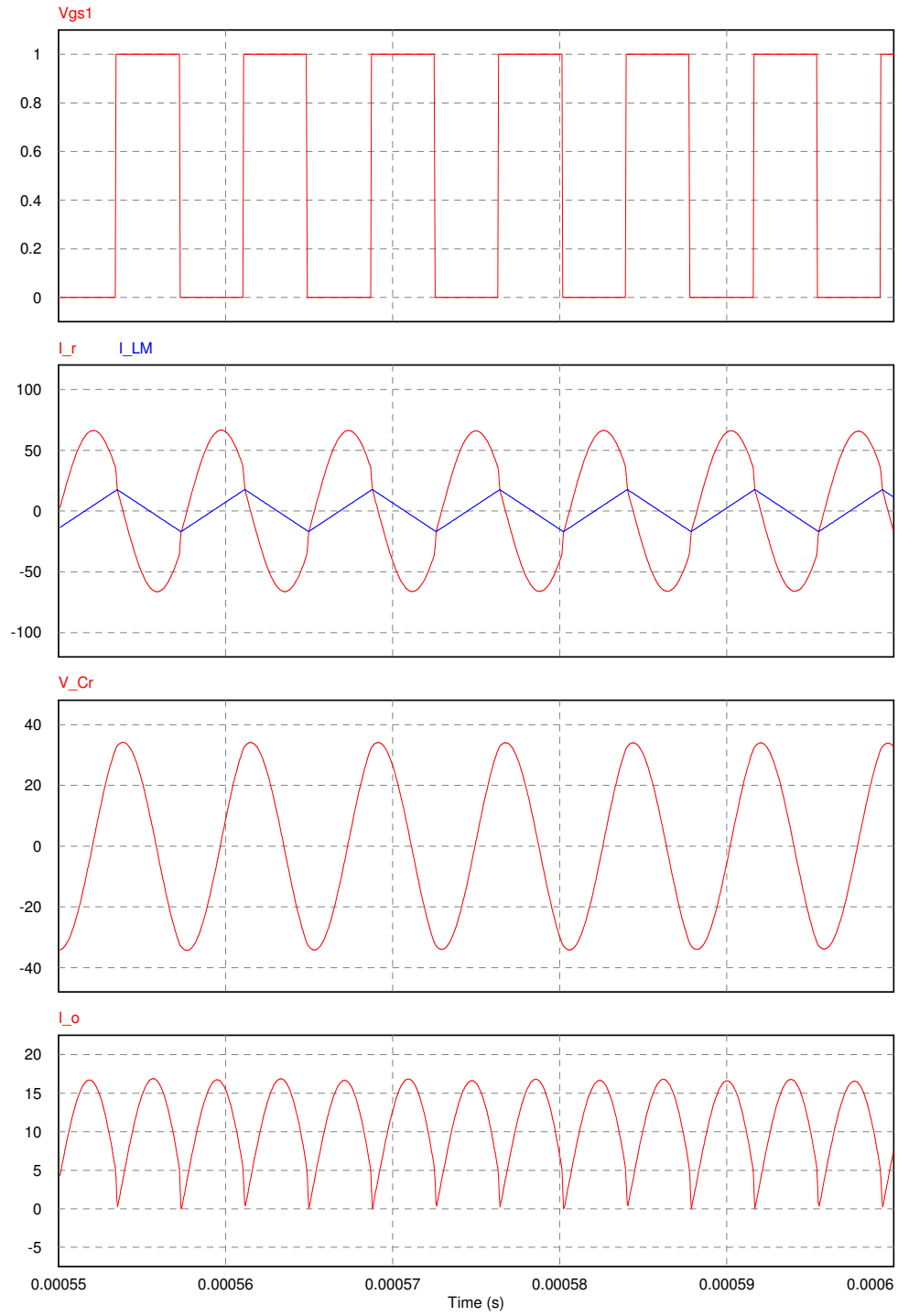


Figure 12: Operation of LLC resonant converter in region 1

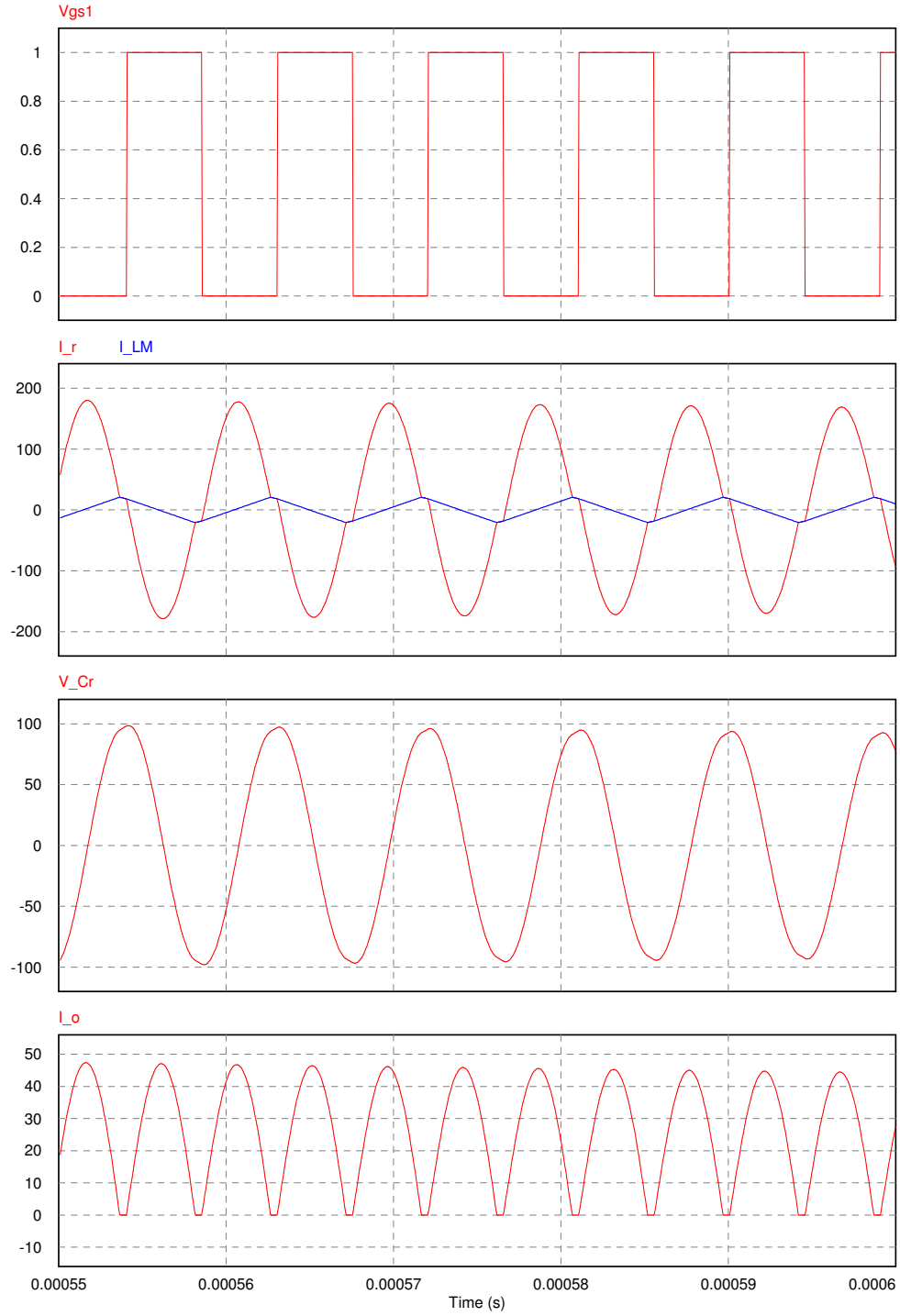


Figure 13: Operation of LLC resonant converter in region 2

3 Control of LLC Resonant Converter

When correctly applied, the application of control theory and feedback can eliminate steady state errors, moderate system sensitivity to parameter changes and disturbances, modify the gain or phase of the system over a desired frequency range, and make unstable systems stable.

For this thesis, the objective is to design a voltage control loop to regulate the output voltage, according to a predefined reference voltage. In other words, regardless of disturbances to the system, and more specifically, the load; the output voltage is to remain at a constant value. Consequently, a negative feedback loop was designed to achieve these specifications.

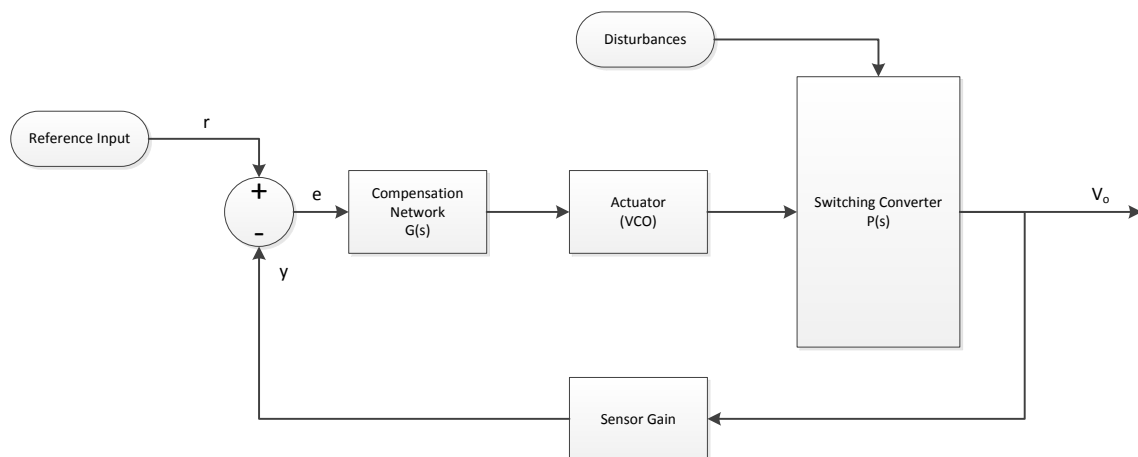


Figure 14: Block diagram of negative feedback loop

From Figure 14, it can be seen that the function of the negative feedback control loop is to determine an input to the plant, such that the desired output behavior can be obtained. Specifically, for the LLC resonant converter, the objective is to generate a set of gate driving signals of frequency f_s for the primary side switch network.

Figure 14 shows that by sensing the output y and comparing it to reference input r , the compensator network $G(s)$ can generate the gate drive signals based on the given error signal e . The error signal is the difference between the y and r , and in a functional control loop, tends to zero after some time period.

3.0.3 Variable Frequency Control

Under normal operating conditions, the LLC resonant converter uses variable frequency control to regulate the output voltage. This type of control requires a gate drive signal that has constant duty cycle, but varying frequency.

To implement variable frequency control, an actuator that can produce a variable frequency signal is required and can be realized by a voltage controlled oscillator (VCO). The VCO is an electronic circuit designed to produce an oscillation frequency based on the control voltage V_{ctrl} and can be implemented as an analog circuit or with a digital signal processor. The relationship between the input signal V_{ctrl} and the output frequency signal ω_o is shown in Equation 11.

$$\omega_o = \hat{\omega} - K_{VCO}V_{ctrl} \quad (11)$$

In Equation 11, $\hat{\omega}$ is the free-running frequency of the VCO, and K_{VCO} is the gain of the voltage controlled oscillator.

3.0.4 Pulse Width Modulation

Pulse-width modulation (PWM) is a fixed frequency control method, and modifies the duty cycle of the pulses to regulate the output voltage. It has been suggested in the literature [16][17] that for light and no load conditions that it may be more effective to control the LLC resonant converter by using PWM rather than variable frequency control. However, in this work, it will be assumed that the converter always operates under nominal loading conditions, and therefore only requires the use of the variable frequency control method.

3.1 Digital Control

Digital controllers have many advantages over analog designs. Digital controllers can be designed to be more robust, and can be easily manipulated for optimal control performance. Additionally, the recent decreases in the cost and size of programmable micro-controllers and digital signal processors (DSP) has made digital control a viable option for power electronics applications.

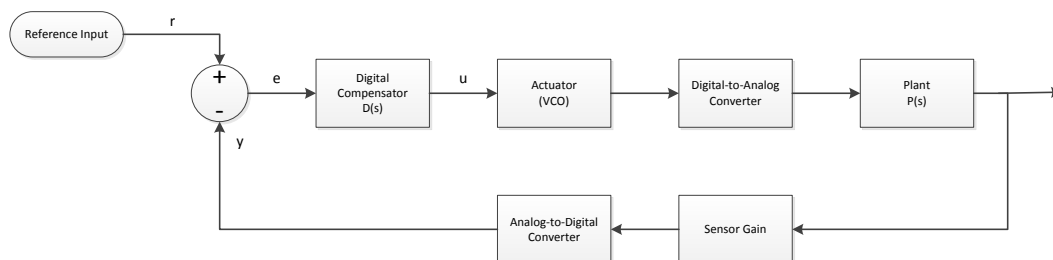


Figure 15: Block diagram of digital negative feedback loop

3.1.1 Effects of Sampling Frequency

An essential consideration that is relevant to digital systems is the principle of sampling, a non-zero timed event to capture the continuous-time data. Sampling is required to convert continuous-time data to discrete-time for processing in the digital signal processor and is physically realized with an analog-to-digital (A/D) converter. The aim of the A/D converter is to accept measured signals from the output of the power electronic converter and then convert these signals into an electrical voltage level that can be read by the DSP. Conversely, once the processing has been completed in the DSP, a digital-to-analog (D/A) converter is used to produce a physical signal to be read by the power electronic converter.

A crucial factor in digital design is the sampling rate at which the continuous-time signal is sampled. Ideally, the sampling rate is infinite such that the discrete-time system is equivalent to the continuous-time model. Unfortunately, since this is not a realistic solution, the alternative solution is to apply the Nyquist rate shown in Equation 12.

$$f_{sample} \geq 2f_{max} \quad (12)$$

The Nyquist rate states that the sampling frequency must be at least twice the maximum bandwidth in the system. By satisfying this criterion, aliasing and signal distortion in the reconstructed signal can be avoided. It can be added that, in fact, it is recommended in [6] to make the sampling frequency ten times the maximum bandwidth.

3.1.2 Design of Digital Control Systems

Digital controllers can be implemented using two primary methods: emulation and direct digital design.

Digital controllers designed through emulation method use the continuous-time plant model, and obtain the compensator model in continuous-time. The continuous-time s-domain model is then converted to a discrete-time z-domain compensator by applying mathematical transformations.

Numerous methods to transform continuous-time transfer functions to discrete-time transfer functions exists. Some typical methods include the Tustin method, zero-order hold, first-order hold, etc. From [18], it was found that for the most accurate models, the first-order hold is the most accurate discretization method, but at the expense of computational complexity. A more general method that is typically used is the zero-order hold discretization as it provides a balance of accuracy and computational efficiency.

The advantage of the emulation method is that well-developed and familiar continuous-time design methods can be applied. This method produces reasonably accurate results given that the sampling rate is very fast. The main disadvantage of the emulation method is that after mapping

the compensator from continuous to discrete-time, it is possible that the control system can no longer achieve the same performance characteristics as in the continuous-time domain model [18].

The other method which can be used to design a digital compensator is by using the direct digital design methodology. Compensators implemented using the direct digital design technique usually have significantly better performance when implemented on digital signal processors. This method of design immediately begins with a plant model already in discrete-time, and then the compensator is designed based off the digitized plant model in the z-domain [19]. Thus, the probability of obtaining unexpected controller response and dynamics are mitigated when the controller is implemented using a DSP.

3.1.3 2-Pole-2-Zero Compensator

Irrespective of which compensator design method is used, the end goal is to design a compensator $G(s)$ to supply the correct signals to maintain output voltage regulation. Loop compensation is achieved by the placement of additional poles and zeros to the feedback system, in conjunction with the system's natural poles and zeros. The system loop gain can then be shaped to the desired performance and stability characteristics by the new poles and zeros introduced to the system. An example of compensator in the digital domain is the 2-pole-2-zero compensator (2P2Z).

The 2-pole-2-zero compensator was selected as the compensator of choice as it can be simply implemented in the z-domain as a difference equation. Its transfer function is given by Equation 13.

$$H_{2p2z}(z) = \frac{b_o + b_1 z^{-1} + b_2 z^{-2}}{1 + a_1 z^{-1} + a_2 z^{-2}} \quad (13)$$

Determining the roots of the quadratic numerator and denominator of Equation 13 gives the location of the zeros and poles of the compensator respectively.

Compared to P, PI, or PID controllers, the 2P2Z compensator allows for five degrees of freedom, and allows for the use of complex poles and zeros [20]. In fact, the P, PI, and PID controllers are simply particular cases of the 2P2Z. For example, the PID controller uses the assumption that the coefficients $a_1 = -1$ and $a_2 = 0$.

$$H_{PID}(z) = \frac{b_o + b_1 z^{-1} + b_2 z^{-2}}{1 - z^{-1}} \quad (14)$$

Furthermore, for implementation in the digital signal processor, the 2P2Z compensator transfer function can be easily re-written in the form of a difference equation.

$$u(k) = b_o e(k) + b_1 e(k-1) + b_2 e(k-2) - a_1 u(k-1) - a_2 u(k-2) \quad (15)$$

A functional block diagram of the 2P2Z is shown in Figure 16.

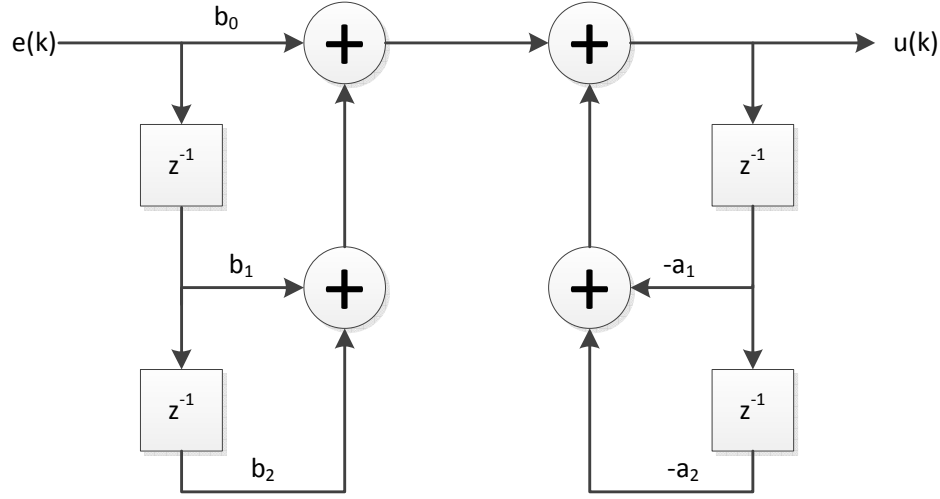


Figure 16: 2 pole 2 zero DSP implementation

3.2 Compensator Design

Two popular methods in which a compensator can be designed for a feedback system are the Bode diagram and root locus.

3.2.1 Root Locus

The root locus method is a plot of all system poles of the closed loop transfer function as some parameter of the system is varied. This design method relocates the closed-loop poles to meet performance specifications such as overshoot, rise and settling times. This method ensures that acceptable transient response characteristics are reached, as well as robust compensator design [21]. A disadvantage of the root locus method is that the system under test must be able to be approximated as a second order system.

3.2.2 Bode Diagram

The Bode diagram displays the magnitude and phase response of a feedback system as two separate plots with respect to the logarithmic frequency [22]. The Bode diagram is useful since the multiplication of transfer functions simply become problems of summation. The phase plot is generally given in degrees ($^{\circ}$) and the magnitude plot is given in decibels (dB) scale.

The conversion of magnitude to magnitude in decibels is given by Equation 16.

$$X_{dB} = 20\log_{10}|X| \quad (16)$$

The performance of compensators designed using the Bode diagram method are based on the bandwidth, gain margin and phase margin [21].

In the Bode diagram, a pole is represented by a 20 dB per decade decay, and a zero is a 20 dB per decade increase.

3.3 Stability

To verify that the designed compensator and plant form a stable system, the stability of the closed loop feedback system can be studied in either the continuous-time domain or the discrete-time domain. The differences in characteristic between the continuous-time and discrete-time domains are discussed in Appendix A.

In this thesis, the stability of the control system will be observed using the Bode and Nyquist diagrams.

3.3.1 Bode Diagram

The stability of the feedback system can be determined from the Bode diagram by observing the gain and phase margins. The phase margin is defined as the phase difference from -180° at the crossover frequency f_c . The crossover frequency is defined as the instance at which the magnitude plot is at unity. The phase margin can be calculated using Equation 17.

$$P.M. = 180 + \angle P(j\omega_{crossover}) \quad (17)$$

The gain margin is the point on the magnitude plot that corresponds to the point on the phase plot at which the phase crosses the -180° axis.

Typically, the target phase margin is between $45^\circ - 60^\circ$, and can be negotiated depending on the requirements for the transient settling time and the stability. For the gain margin, it is generally accepted that good gain margin is greater than 9 dB [23].

3.3.2 Nyquist Plot

Alternatively, the stability of the system can be observed using the Nyquist plot. The Nyquist plot displays the frequency response as a single plot in the complex plane, and is a graphical representation of the loop transfer function as $j\omega$ traverses the contour map [24].

Stability in the Nyquist plot can be observed by applying the Nyquist stability criterion. This criterion is determined by examination of the enclosure around the critical point $(-1, 0)$. For closed loop stability, the Nyquist plot must encircle the critical point once for each right hand pole, in a direction that is opposite to the contour map [24].

It would be appropriate and useful to relate the Nyquist stability criterion to the Bode diagram magnitude and phase plots [25]. There are two main relationships that can be made:

- The unit circle of the Nyquist plot is equivalent to the 0 dB line of the magnitude plot.
- The negative real axis of the Nyquist plot is equivalent to the -180° phase line of the phase plot.

4 Implementation and Verification

In this thesis, the plant process is given by the ratio of the output voltage to the switching frequency, and is expressed in Equation 18. Since it was determined that the direct digital design method gives superior results, it is the selected method for the design of the compensator.

$$P(s) = \frac{V_o}{f_s} \quad (18)$$

Consequently, the first step is to obtain a description of the plant process model, in either continuous or discrete time, which can be discretized so that the compensator may be directly designed in the discrete-time z-domain.

However, since the mathematical relationship described by Equation 18 is not well-defined in the literature, one proposed solution is to measure the frequency response of the LLC resonant converter using a network analyzer. The frequency response can be obtained by probing the output voltage, and the switching frequency while the switching frequency is undergoing small signal perturbations around a designated operating point.

This methodology has the main advantage of capturing the true behavior and dynamics of the LLC resonant converter, as well as any additional behaviors that appear due to parasitic components. This measurement method provides the most realistic representation of the plant process model, however it assumes a prototype model has already been designed and is functional.

4.1 Design Methodology

4.1.1 Overview

The approach taken to design the digital controller was to first use a laboratory bench prototype model and network analyzer to obtain the frequency response data of the plant process model. Different loading conditions were then applied to the prototype model to observe the changes in the frequency response. Additionally, bench data of the DC gain characteristics under different loading conditions were obtained to compare with the theoretical models presented in Chapter 2.

The obtained frequency response data of the physical plant model was then imported into the MATLAB[®] environment, and based on the obtained data, a compensator was designed in MATLAB[®]. To verify that the compensator design is satisfactory, the designed compensator coefficients can be extracted from MATLAB[®], and then exported to a software more suitable for power electronics simulation.

Finally, an example implementation using a Texas Instruments[®]-based digital signal processor (DSP) is given.

4.1.2 Bench Test Results

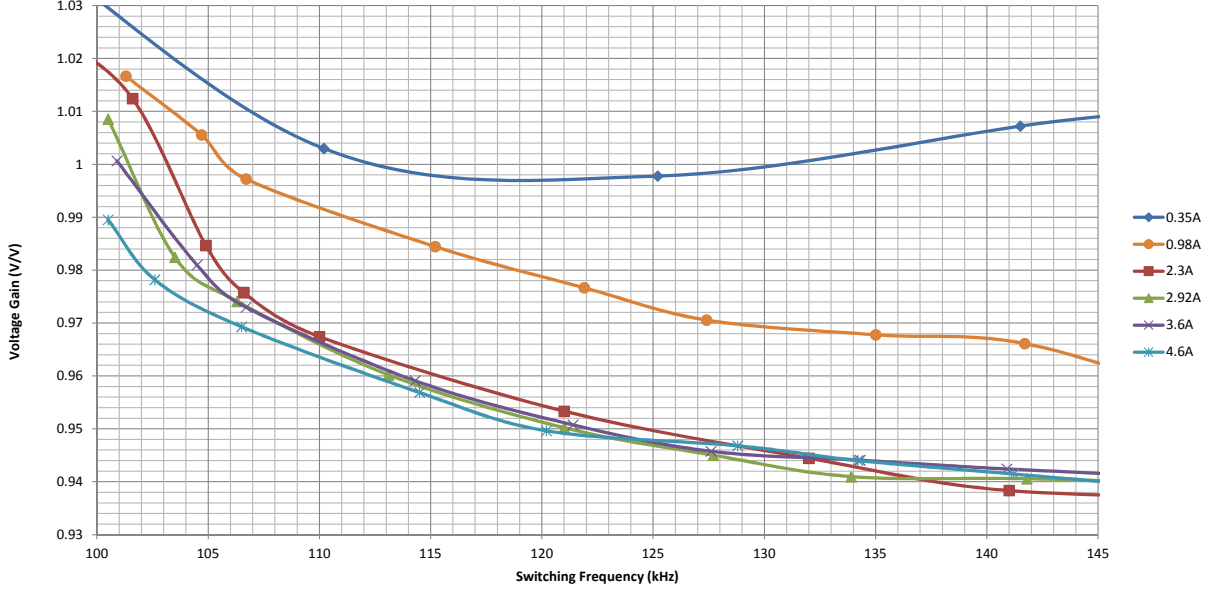


Figure 17: Bench test result of DC gain characteristic for Region 1

Figure 17 shows the DC voltage gain characteristic of the prototype model when operated above the resonant frequency. From these results, it is evident that for light loading conditions, the LLC resonant converter begins to display non-linear characteristics, which suggests a separate control loop may be necessary for light load operation. For loading conditions approaching the nominal load, it appears that the prototype model follows the theoretical DC gain characteristics as given by Figure 4b. Figure 17 also shows that the boundary condition between nominal and light loading conditions for this particular converter lies around 2.3 A.

Given that the resonant frequency is the quiescent operating point, Figure 18 shows the frequency response of the prototype model with different loading conditions. Figure 18 plots the magnitude of the ratio between the output voltage and control voltage in decibels (dB) with respect to the relative frequency in Hertz (Hz). From these results, it was determined that the frequency response of the plant model also has a large dependency on the loading conditions.

Since there may be frequent changes to the load, the compensator design should be based on the plant process model that represents the worst-case scenario. For this thesis, it will be assumed that the converter is operated under nominal operating conditions, and thus, the worst-case is defined as the loading condition such that the phase margin is minimum, as this is the condition that is

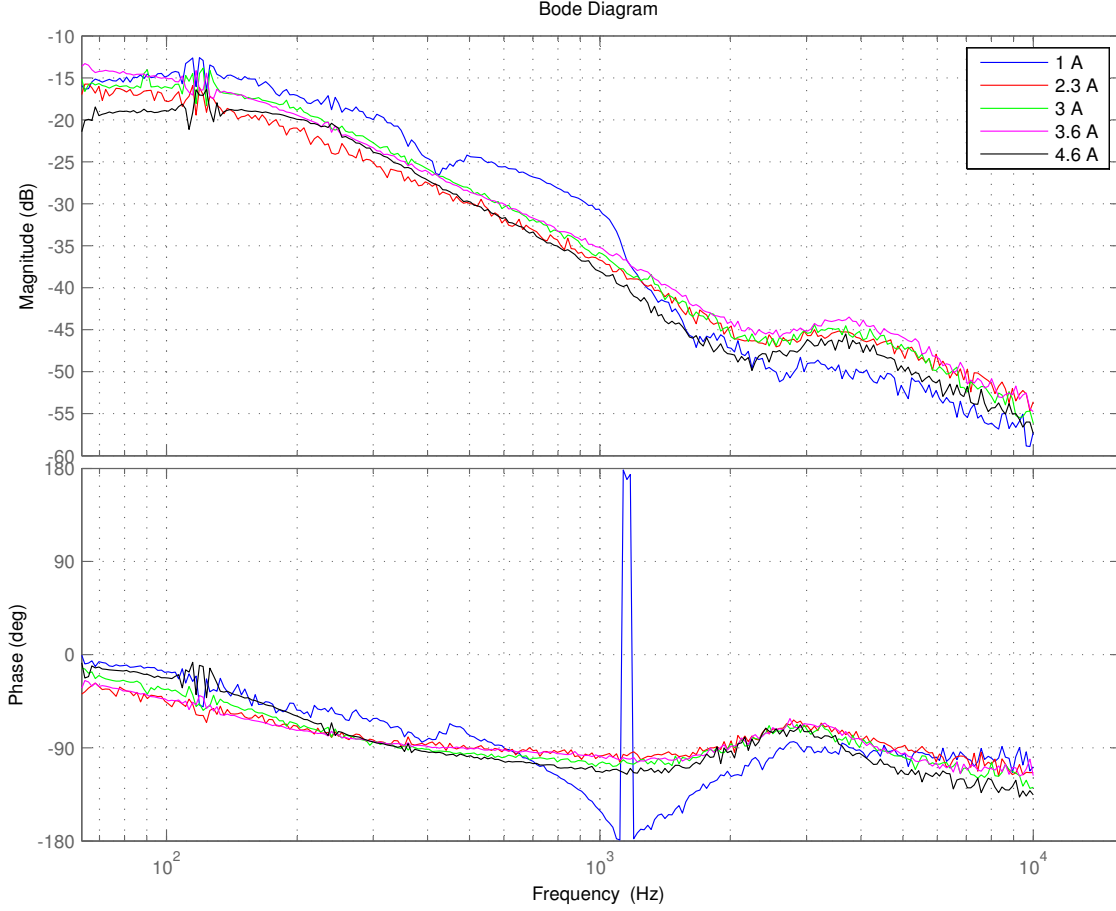


Figure 18: Plot of relative frequency response of prototype model under different loading conditions

most likely to be overcome by problems of instability. In Figure 18, this scenario is represented by the curve '4.6 A.'

It can be noted that the frequency response generally follows the form of a low-pass filter (LPF), with the addition of a high frequency pole-zero combination. Because this system appears to be greater than second order, design of the compensator using the Bode diagram technique is preferred over other design methods.

4.1.3 Compensator Design Results

MATLAB® has several useful tools for digital controller development. Firstly, built-in functions such as '*c2d*' make it straightforward to convert continuous-time s-domain models to discrete-time z-domain models. Secondly, the Control System Toolbox features the SISO Design Tool which

allows for simple, visual design of control systems.

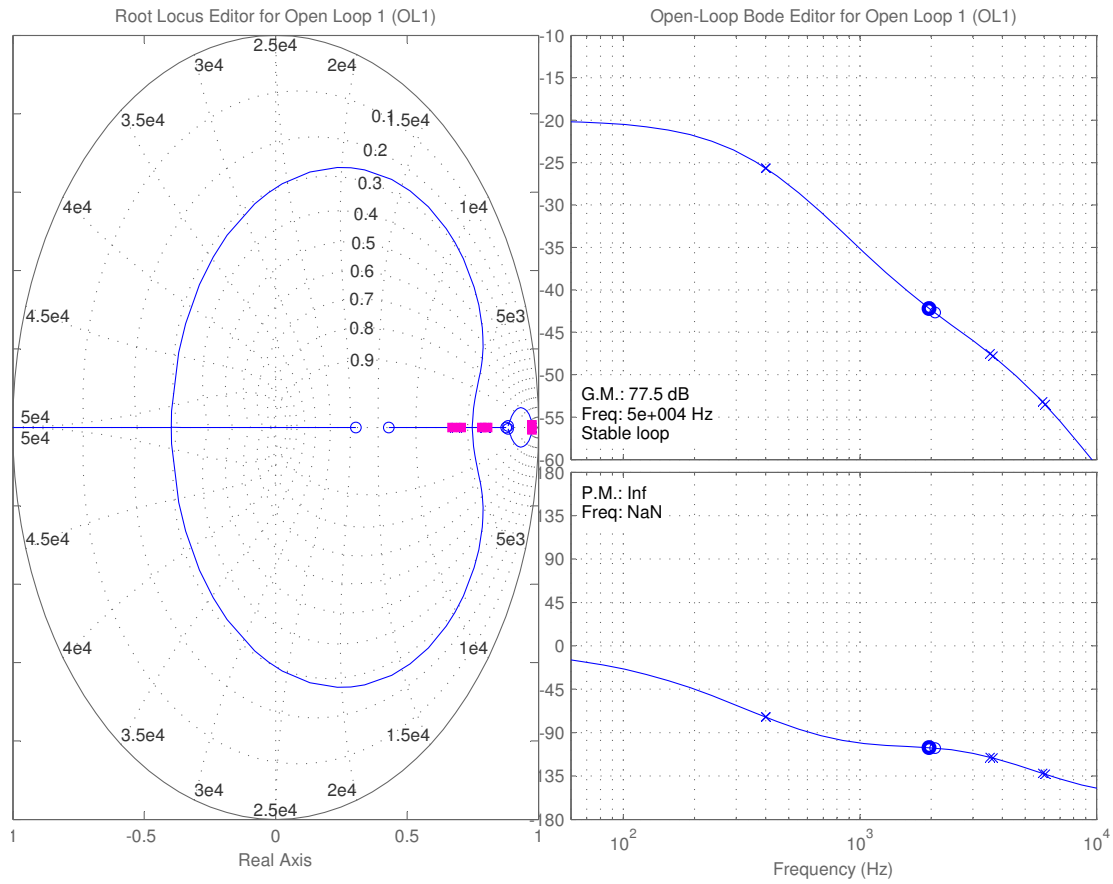


Figure 19: Prototype model frequency response data in MATLAB® SISOTOOL GUI environment

In this case, the frequency response data of the plot ‘4.6 A,’ a continuous-time domain function, is transformed into a discrete-time z-domain frequency response plot with the ‘*c2d*’ command and an appropriate sampling time.

With the z-domain frequency response in hand, the ‘*sisotool*’ command opens the SISO Design GUI for interactive compensator design, and allows for controller design using root locus, Bode diagram, and Nichols techniques.

Using the Bode diagram design editor, the ‘*sisotool*’ GUI environment allows the user to manually add and position the poles and zeros of the compensator according to the specifications required for the control system [26]. The bandwidth, gain and phase margins, as well as the closed-loop step response can then be easily obtained from the GUI environment to verify the stability and performance of the designed compensator model.

Figure 20 shows the response of the open-loop system with the designed digital compensator. The open loop response appears to be stable and has a gain and phase margin of 53.8 dB and 60° respectively.

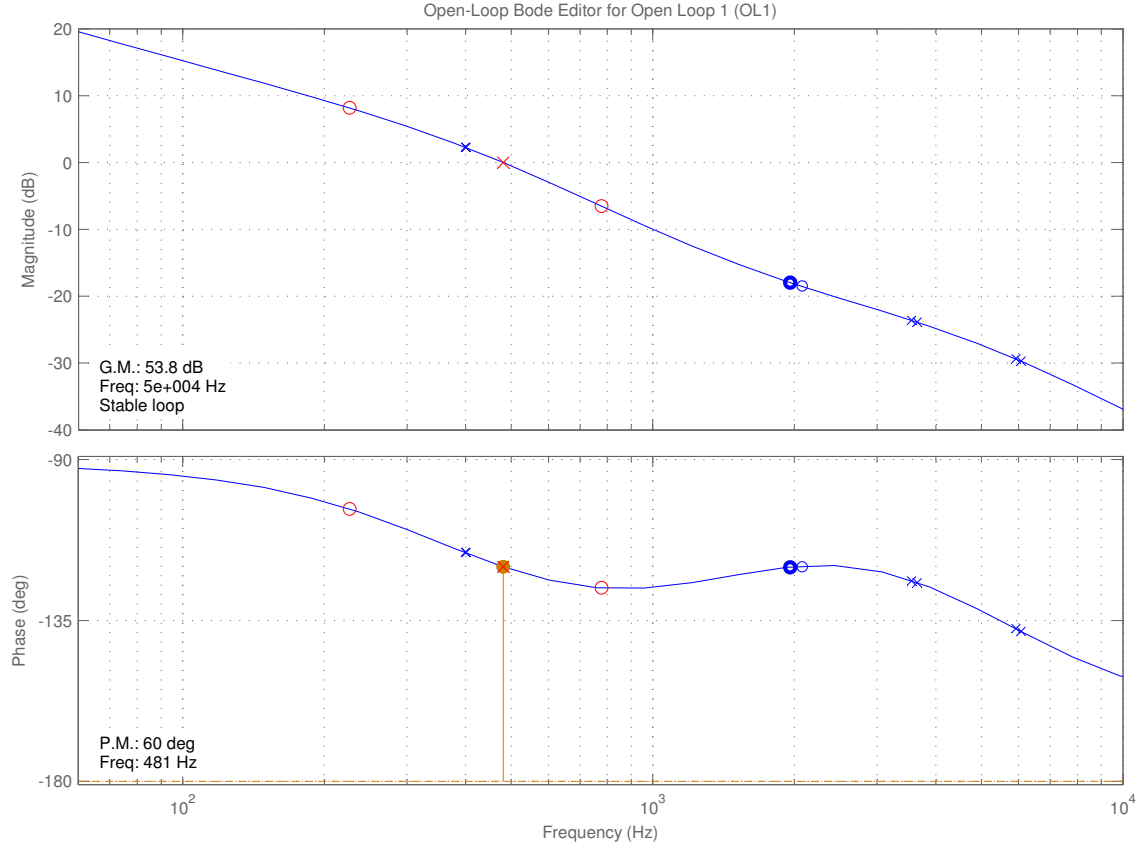


Figure 20: Open-loop Bode plot of prototype frequency response data

Given that a step change to the control voltage input is applied to the system, the closed-loop step response of the system is given by Figure 21, and shows a rise time of approximately 1 ms, and after 2.5 ms, the steady state error is reduced to zero. The overshoot of the step response is approximately 10%.

From the results of Figure 20 and Figure 21, it appears that a stable compensator with appropriate gain and phase margin has been designed. Since these results appear to be reasonable, the designed compensator coefficients can be exported to the PSIM[®] simulation model for verification.

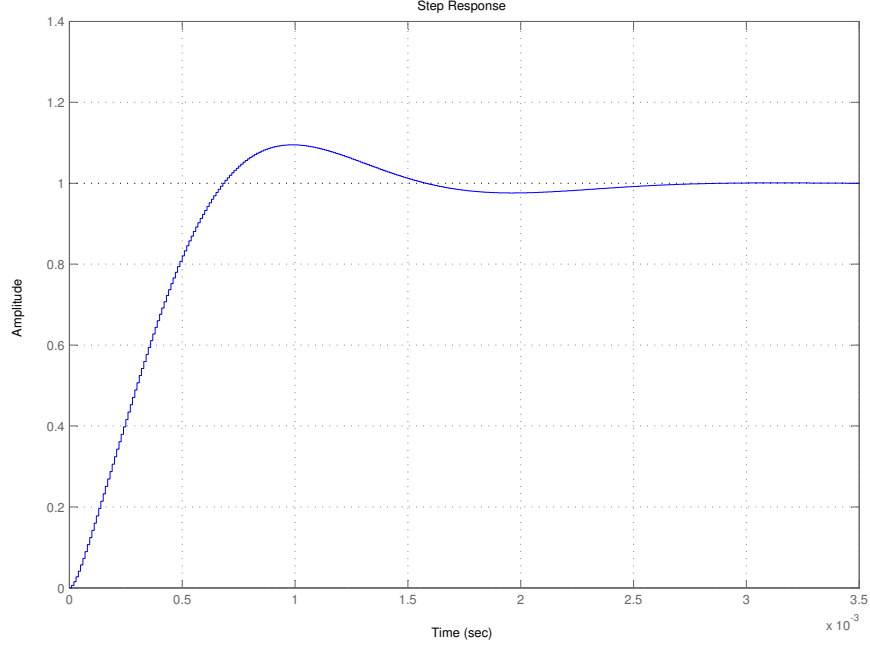


Figure 21: MATLAB® step response of closed-loop system using prototype model

4.1.4 Verification in PSIM®

The negative feedback control loop of Figure 15 was implemented and simulated using Powersim's PSIM® simulation software, a software specifically designed for power electronics simulation [27]. The simulation file includes a model of the LLC resonant converter in a negative feedback loop configuration. Additionally, to more closely model the effects of the DSP circuit, the sample-and-hold, and quantization effects of the analog-to-digital converter are also included in the model. As seen in [28], the A/D converter can be approximately modelled as an ideal switch switching at frequency f_{sample} and a zero-order hold (ZOH) block. It will be assumed that the sampling rate is high enough such that the sampling can be considered ideal. Additionally, a quantization block been included to simulate the quantization error during typical A/D conversion [27].

The complete circuit schematic of the PSIM® simulation model is shown in Figure 22, and the controller components are shown in Figure 23. The model of the 2P2Z compensator is implemented in the difference equation format according to Figure 16, and the VCO actuator is designed according to Equation 11.

In the simulation, the reference set point value of the voltage control loop was set to be 190 V. Figure 24 shows that the steady-state value of the error voltage approaches zero, and confirms that the controller meets the output regulation requirement.

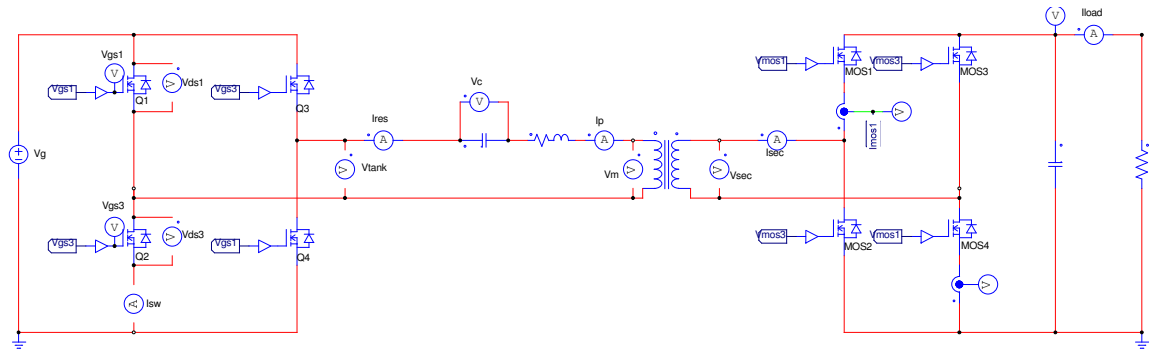


Figure 22: PSIM® circuit schematic of LLC resonant converter

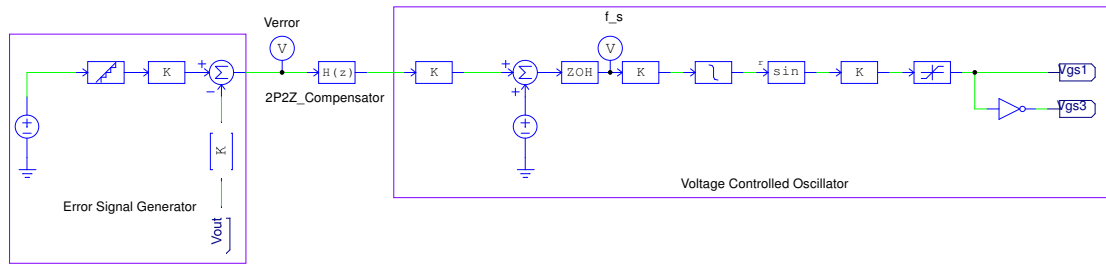


Figure 23: PSIM® controller schematic of LLC resonant converter

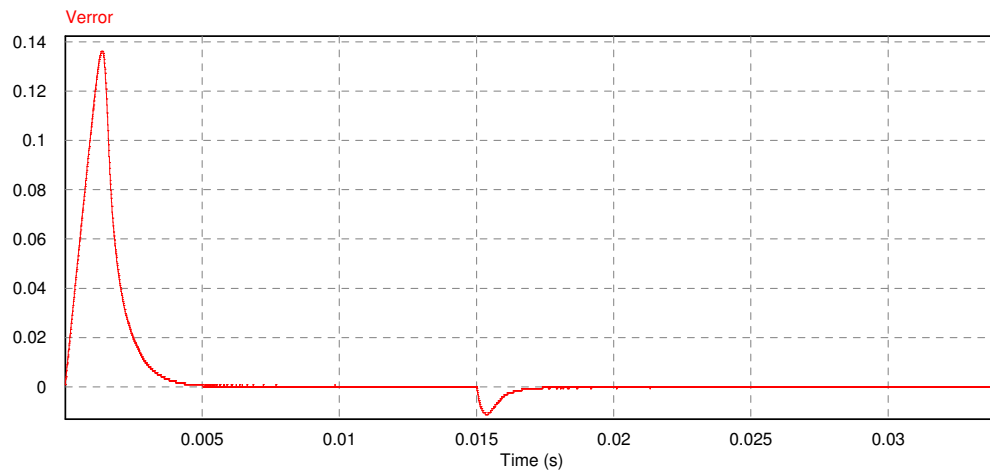


Figure 24: Error voltage of prototype model

A study of the effects of a steady-state load step change are shown in Figure 26. A step load change in the simulation is applied at $t = 15\text{ms}$, and from the results of Figure 26, it has been verified that the designed control system that has been implemented is functional and is able to maintain output voltage regulation even when undergoing changing loading conditions. As expected, the switching frequency f_s increases when the load was decreased. Figure 26 also shows the response of the current through the resonant tank, and the switching frequency.

For interest, the ripple voltage of the output voltage was also observed and was found to be approximately 1.4 mV and is shown in Figure 25.

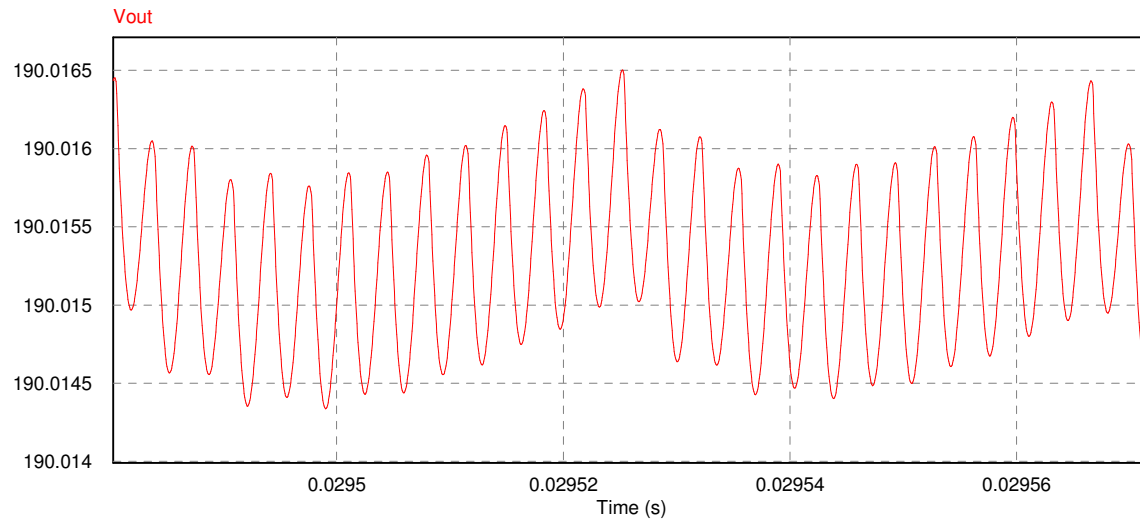


Figure 25: Output voltage ripple of prototype model

The results of the simulation are summarized in Table 1. Based on the final results, it can be concluded that a sufficient digital controller has been designed to achieve output regulation.

Output voltage value:	190 V
Steady-state error:	0 V
Output voltage ripple	1.4 mV
% overshoot:	10%
Rise-time:	1 ms
Settling-time:	2.5 ms

Table 1: Results of prototype model

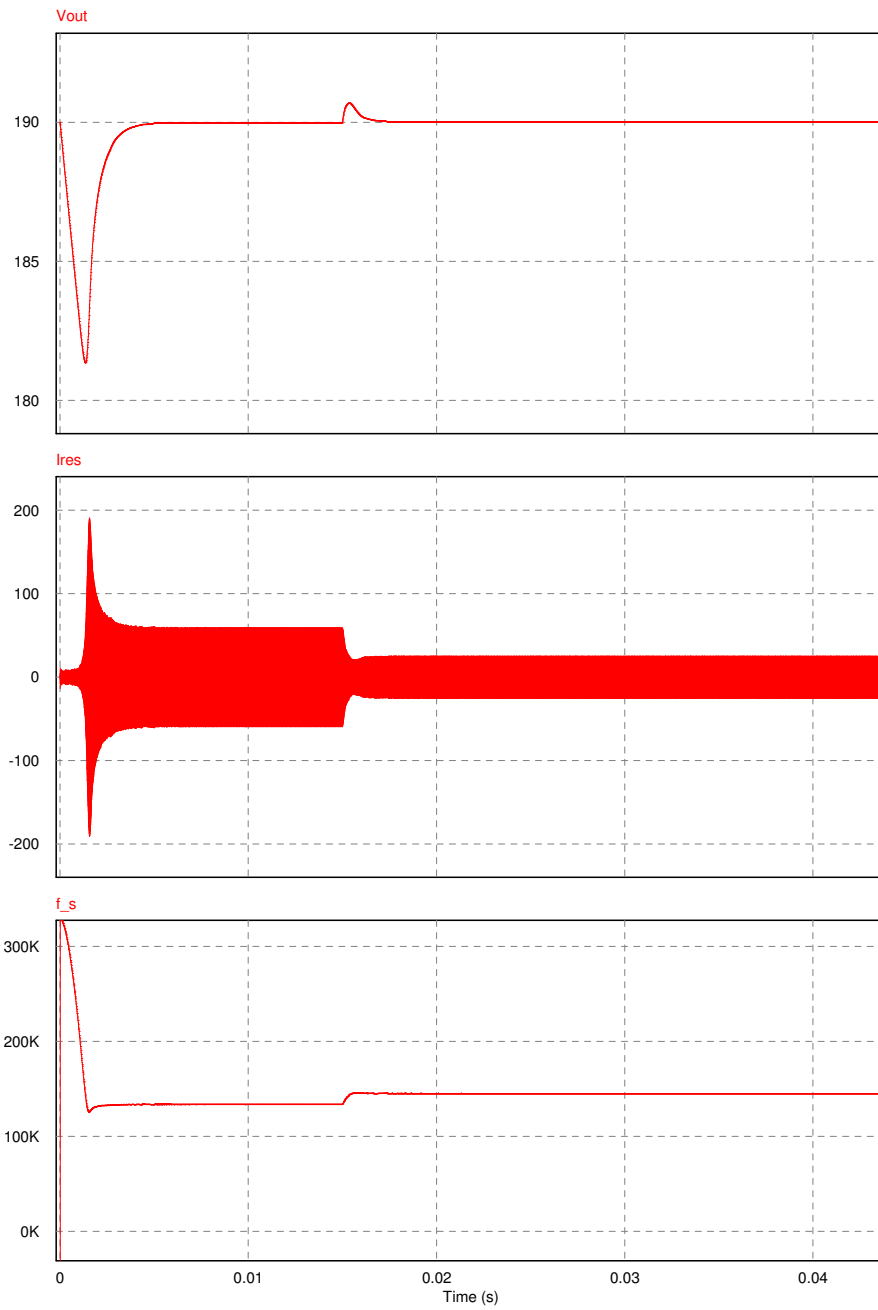


Figure 26: PSIM® closed-loop response to step load change using prototype model

4.2 Texas Instruments[®] DSP

To implement the voltage control loop digitally, a DSP is required. Texas Instruments[®] (TI) has a large portfolio of micro-controllers and digital signal processors available for use.

In this thesis, the TMS320F28035 Piccolo was selected as the ideal digital signal processor as it has the capability to use both the on-board central processing unit (CPU) as well as the additional Control Law Accelerator[™] (CLA) platform. The CLA has the advantage of minimizing the processing latency of regular DSPs since it can execute time-critical control algorithms in parallel with the main CPU [29].

The voltage control loop can be implemented onto the CLA partition of the TMS320F28035 DSP using assembly language programming. To assist with the programming related to the CLA, the controlSUITE[™] package offered by TI provides many example code snippets for use.

Figure 27 shows an algorithm that can be used to implement the voltage control loop with the CLA.

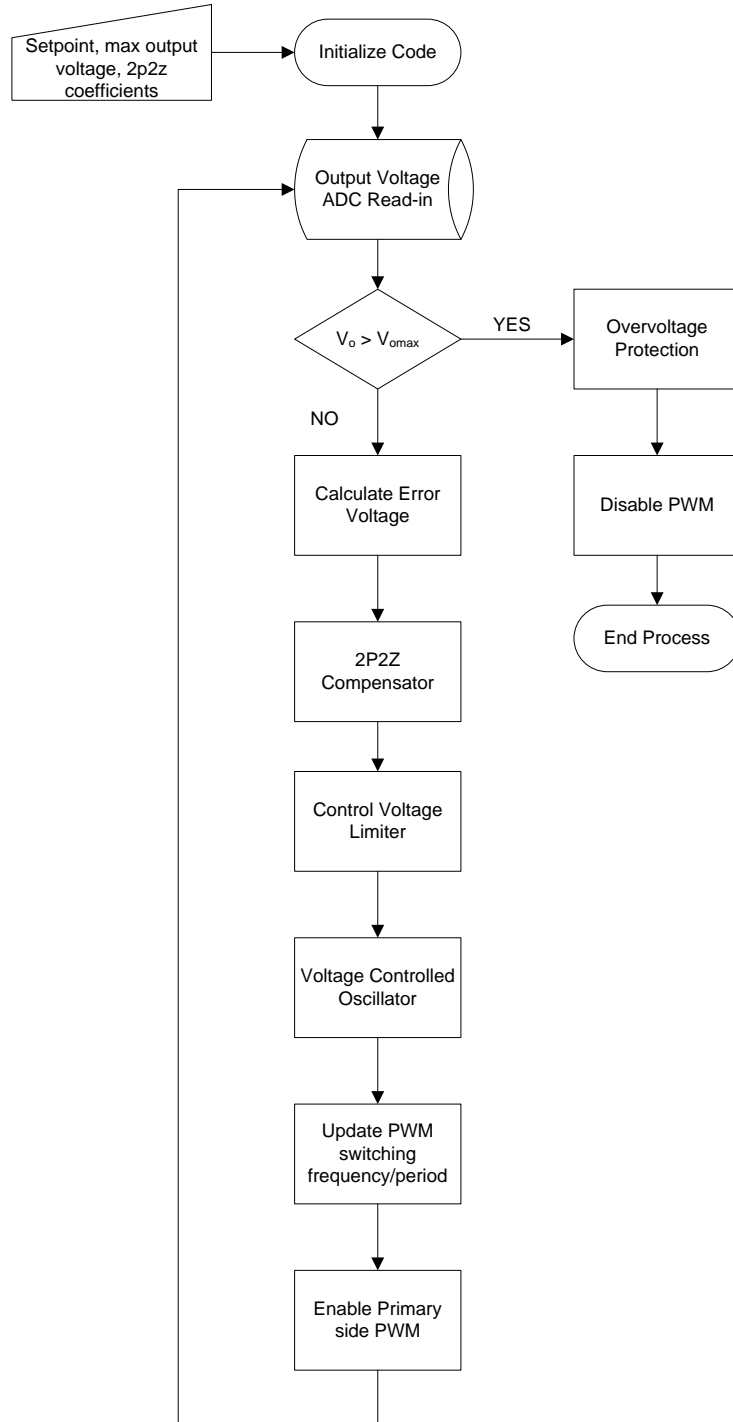


Figure 27: Voltage loop flow diagram for DSP implementation

5 Derivation of Control-to-Output Transfer Function

5.1 Overview

The control-to-output transfer function of the LLC resonant converter represents the ratio of the output voltage V_o to small signal variations in the switching frequency f_s . The difficulty in designing compensators for the LLC resonant converter lies in the fact that there are few known examples in literature of the control-to-output transfer function, which in this case represents the plant process model of the control loop.

Modelling the small signal characteristics of the LLC resonant converter is particularly difficult because many averaging techniques, such as state space models cannot be used. In [7] and [30], it is noted that unlike PWM converters, the control-to-output transfer of the converter cannot be obtained by the state space averaging methods, due to the way energy is processed in the LLC resonant converter.

Currently, most known applications ([30][31]) rely on bench measurements and frequency response data to help determine the plant process model for the design of the compensation network. In practice, the transfer function can be obtained by using a network analyzer to measure the frequency response of the plant process model, and then using the data to design the compensator. This methodology has the inherent disadvantage of requiring a pre-built functioning prototype model.

A proposed control-to-output transfer function that does not use frequency response data was presented in [32]. It was proposed that the control-to-output transfer function could be approximated as a third order polynomial. However, for the transfer function to be computed, variables such as the damping factor and the beat frequency of the converter need to be known. Additionally, a third order polynomial equation would not be able to predict the high frequency pole-zero shown in Figure 32.

Finally, similar to the method proposed in [7], computer simulation can also be used. The difficulty in creating a simulation model that can accurately model the true component and parasitic models may be difficult. With digital controllers, computer simulation is further complicated since the modelling of the effects of the DSP hardware can only be approximated. Additionally, as noted in [7], the computer simulation method requires extensive computing power.

5.2 Transfer Function Derivation

In the proceeding sections, a novel model of the small signal characteristics of the control-to-output transfer for the LLC resonant converter will be presented. A MATLAB[®]-based software program has been developed to determine the frequency response of the derivation results, and will be compared to the frequency response data obtained in Chapter 4.

As per Chapter 2, resonant converters that utilize variable frequency control regulate the output voltage by supplying sinusoids of different frequencies to the input of the resonant tank. The effect of this is to alter the tank impedance, and thus control the voltage drop across the resonant tank. Generating the appropriate sinusoid is accomplished by varying the switching frequency of the primary side switch network.

In order to develop a method to calculate the small signal control-to-output transfer function of the LLC resonant converter, techniques borrowed from communications theory can be used. More specifically, the operation and analysis of the converter can be described by using analogies similar to that of frequency modulation (FM), as well as amplitude modulation (AM).

The generalized block diagram shown in Figure 28 shows the steps of the analysis that will be taken for the development of the derivation model.

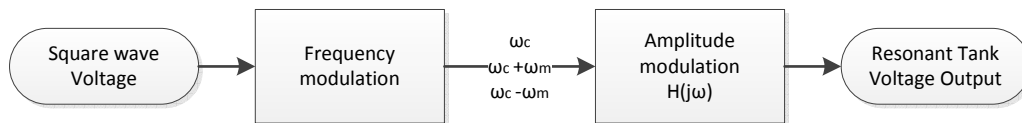


Figure 28: Analysis road map

5.2.1 Frequency Modulation

Recall that the general equation for a sinusoid is given by

$$v(t) = A \cos(\phi(t)) \quad (19)$$

Frequency modulation is defined as a deviation in frequency from the carrier signal frequency. Mathematically, this deviation in frequency can be expressed as the addition of an additional cosine term to the carrier frequency [33]. The radial frequency of a signal undergoing frequency modulation can be expressed as

$$\omega_s(t) = n\omega_c t + \Delta\omega \cos(\omega_m t) \quad (20)$$

In the above equation, $\Delta\omega$ is defined as the amplitude of the deviation from the carrier frequency, and ω_m , the modulating frequency, is defined as the rate of carrier deviation.

To arrive at an equation that can be substituted into Equation 19, the following relationship between the angular velocity $\omega_s(t)$ and the angle $\phi(t)$ is used.

$$\phi(t) = \int \omega_s(t) dt \quad (21)$$

$$\phi(t) = n\omega_c t + \frac{\Delta\omega \sin(\omega_m t)}{\omega_m}$$

In the scope of this thesis, it is known that the deviation is actuated by a voltage controlled oscillator and $\Delta\omega$ can be substituted by

$$\Delta\omega = 2\pi K_{VCO}\epsilon \quad (22)$$

where K_{VCO} is the gain of the voltage controlled oscillator, and the amplitude of the applied small signal perturbation is given by the constant ϵ .

Therefore, Equation 21 can be expressed as

$$\phi(t) = 2\pi \left(n f_c t + \frac{K_{VCO}\epsilon \sin(\omega_m t)}{\omega_m} \right) \quad (23)$$

To simplify Equation 23, the modulation index β can be substituted and is defined as

$$\beta = \frac{2\pi K_{VCO}\epsilon}{\omega_m} \quad (24)$$

5.2.2 Square Wave Approximation

The aforementioned mathematical relationships give a description of the effects of frequency modulation on the carrier frequency. However, prior to applying the above equations for use in analysis, the form of the original unmodulated signal must be determined.

The aperiodic square wave waveform is supplied from a DC voltage source and is produced as a result of switching complementary pairs of field effect transistor (FET) switches in the primary side FET bridge. Mathematically, a generic square wave signal undergoing frequency modulation is given as

$$V_s(t) = \sum_{n=1,3,5,\dots}^{\infty} \frac{4V_g}{n\pi} \sin(n2\pi f_c t + \beta \sin(\omega_m t)) \quad (25)$$

In [7], it is acknowledged that analysis including harmonics up to the fifth harmonic may be useful in modelling the control-to-output transfer function of the LLC resonant converter. Computer simulations recorded in [7] show that by including the harmonic content, the accuracy of the models are improved.

The model proposed in this thesis includes the third and fifth harmonics, in addition to the fundamental frequency of the square wave waveform. By including the third and fifth harmonics in the model, a more accurate understanding of the true dynamics of the converter can be observed. Additionally, the effects of including supplementary sideband frequencies (for the case where $|\beta|$ does not meet the condition $|\beta| \ll 1$) are studied and included in the new model.

Equation 25 is therefore defined as

$$\begin{aligned} V_s(t) = & \frac{4V_g}{\pi} \sin(\omega_c t + \beta \sin(\omega_m t)) \\ & + \frac{4V_g}{3\pi} \sin(3\omega_c t + \beta \sin(\omega_m t)) \\ & + \frac{4V_g}{5\pi} \sin(5\omega_c t + \beta \sin(\omega_m t)) \end{aligned} \quad (26)$$

For simplicity, each individual harmonic component is redefined as $V_{s1}(t)$, $V_{s3}(t)$, and $V_{s5}(t)$.

5.2.3 Bessel Functions of the First Kind

To gain better insight to the effects of frequency modulation, Bessel functions are used to determine the amplitudes of the carrier and resulting sideband frequencies.

Expanding Equation 26 by using Bessel functions has the advantage of determining the locations of the modulated frequencies in the frequency spectrum, as well as giving the amplitude of each frequency component. As an example, $V_{s1}(t)$ can be expanded using Bessel functions and is given by

$$\begin{aligned} V_{s1}(t) = & J_0(\beta) \frac{4V_g}{\pi} \sin(\omega_c t) \pm J_1(\beta) \frac{4V_g}{\pi} \sin((\omega_c \pm \omega_m)t) \\ & \pm J_2(\beta) \frac{4V_g}{\pi} \sin((\omega_c \pm 2\omega_m)t) \pm \dots \pm J_n(\beta) \frac{4V_g}{\pi} \sin((\omega_c \pm n\omega_m)t) \end{aligned} \quad (27)$$

$J_n(\beta)$ is denoted as a Bessel function of the first kind and can be calculated by

$$J_n(\beta) = \sum_{m=0}^{\infty} \frac{(-1)^m}{m! \Gamma(m+n+1)} \left(\frac{\beta}{2} \right)^{2m+n} \quad (28)$$

In Equation 28, the variable n is the n^{th} sideband frequency, and β is the modulation index. In lieu of Equation 28, there are existing tables developed in [34], which can be used to determine corresponding values of $J_n(\beta)$ given the value of β .

In [35], there is an assumption that the value of $|\beta|$ is much less than one. This is normally a useful assumption as the following simplifications of the Bessel functions become valid.

$$J_0(\beta) \approx 1 \quad (29)$$

$$J_n(\beta) \approx \frac{\beta^n}{n!2^n}$$

As can be seen in Equation 29, for values of β much less than one, higher order sideband frequencies will be approximately equal to zero.

However, since the assumption that β is much less than one is not always valid, the use of Equation 29 is quite restrictive. Therefore, in this thesis, the assumption of $|\beta|$ being much less than one is not used. Instead, the values of $|\beta|$ are determined and calculated in MATLAB® with the function ‘*besselj*’. This function is based on the tables found in [34].

Since the $|\beta|$ value is no longer assumed to be small, the higher order values of $J_n(\beta)$ become significant. Therefore, the n^{th} highest sideband to be considered remains to be determined.

It is known that the number of sidebands for the fundamental and harmonic components are determined by the value of the modulation index β . Theoretically, under frequency modulation, there are an infinite number of sideband frequencies, and therefore, a finite number of sideband frequencies must be selected in a way such that the majority of the signal’s energy is captured.

According to Equation 24, β is inversely proportional to ω_m . From this, the conclusion can be drawn that as ω_m increases, the modulation index becomes small, and the total number of sideband frequencies is reduced.

Therefore, it can be said that the "worst-case" is the scenario when ω_m is at its smallest value, such that the value of $|\beta|$ becomes large. For the purpose of this thesis, the value of ω_m is taken to be located at 1000π rad/s. By setting ω_m to 1000π rad/s, a corresponding value of β is determined, and the number of sidebands required can also be determined.

To verify that there are a sufficient number of sideband frequencies, the sideband frequencies that account for 99% of the signal energy (in the pre-determined worst case) are considered.

The energy of a carrier and sideband signals is determined by

$$E = J_0(\beta)^2 + \sum_{n=1}^x 2(J_n(\beta))^2 \quad (30)$$

To determine how many sidebands are needed to have 99% of the signal energy, an increasing number of sidebands x is added to the carrier frequency amplitude until the value of E is equal to 0.99.

It was determined that by including three pairs of symmetrical sideband frequencies to the fun-

damental, third and fifth harmonic components, that 99% of the signal energy would be accounted for the case where ω_m is greater than 1000π rad/s. Thus, Equation 27 can be written as

$$\begin{aligned}
V_{s1}(t) = & J_0(\beta) \frac{4V_g}{\pi} \sin(\omega_c t) \pm J_1(\beta) \frac{4V_g}{\pi} \sin((\omega_c \pm \omega_m)t) \\
& \pm J_2(\beta) \frac{4V_g}{\pi} \sin((\omega_c \pm 2\omega_m)t) \pm J_3(\beta) \frac{4V_g}{\pi} \sin((\omega_c \pm 3\omega_m)t)
\end{aligned} \tag{31}$$

5.2.4 Amplitude Modulation

Each individual frequency component is then passed through and filtered by the resonant tank circuit at their respective frequencies. This is equivalent to amplitude modulation (AM) and is mathematically equivalent to multiplying each frequency component with the resonant tank transfer function at the corresponding frequency. The resulting signal represents a voltage, that will be eventually applied to the secondary side of the converter.

As an example, the carrier, upper and lower sideband frequencies of the third harmonic undergoing amplitude modulation are given by Equations 32 - 38. Similar equations can be determined for the fundamental and fifth harmonic components.

$$V_{s3,carrier} = J_0(\beta) \times \frac{4V_g}{3\pi} \sin(3\omega_c t) \times H(3j(\omega_c)) \tag{32}$$

$$V_{s3,upper1} = J_1(\beta) \times \frac{4V_g}{3\pi} \sin((3\omega_c + \omega_m)t) \times H(j(3\omega_c + \omega_m)) \tag{33}$$

$$V_{s3,lower1} = -J_1(\beta) \times \frac{4V_g}{3\pi} \sin((3\omega_c - \omega_m)t) \times H(j(3\omega_c - \omega_m)) \tag{34}$$

$$V_{s3,upper2} = J_2(\beta) \times \frac{4V_g}{3\pi} \sin((3\omega_c + 2\omega_m)t) \times H(j(3\omega_c + 2\omega_m)) \tag{35}$$

$$V_{s3,lower2} = -J_2(\beta) \times \frac{4V_g}{3\pi} \sin((3\omega_c - 2\omega_m)t) \times H(j(3\omega_c - 2\omega_m)) \tag{36}$$

$$V_{s3,upper3} = J_3(\beta) \times \frac{4V_g}{3\pi} \sin((3\omega_c + 3\omega_m)t) \times H(j(3\omega_c + 3\omega_m)) \tag{37}$$

$$V_{s3,lower3} = -J_3(\beta) \times \frac{4V_g}{3\pi} \sin((3\omega_c - 3\omega_m)t) \times H(j(3\omega_c - 3\omega_m)) \tag{38}$$

The Euler formula is useful in this case, and is given by

$$\sin(\theta) = \frac{e^{j\theta} - e^{-j\theta}}{j2} \quad (39)$$

Applying Equation 39 to the trigonometric term of the resonant tank outputs, the above equations can be rewritten. As an example, the equations of the carrier and sideband frequencies for the third harmonic are shown in Equations 40 - 46. The equations for the fundamental and fifth harmonic components can be determined similarly.

$$V_{s3,carrier} = \frac{B_o e^{j3\omega_c t} - B_o^* e^{-j3\omega_c t}}{j2} \quad (40)$$

$$V_{s3,upper} = \frac{(B_u e^{j3\omega_m t}) e^{j3\omega_c t} - (B_u e^{j\omega_m t})^* e^{-j3\omega_c t}}{j2} \quad (41)$$

$$V_{s3,lower} = \frac{(B_l e^{-j\omega_m t}) e^{j3\omega_c t} - (B_l e^{-j\omega_m t})^* e^{-j3\omega_c t}}{j2} \quad (42)$$

$$V_{s3,upper2} = \frac{(B_{u,2} e^{j2\omega_m t}) e^{j3\omega_c t} - (B_{u,2} e^{j2\omega_m t})^* e^{-j3\omega_c t}}{j2} \quad (43)$$

$$V_{s3,lower2} = \frac{(B_{l,2} e^{-j2\omega_m t}) e^{j3\omega_c t} - (B_{l,2} e^{-j2\omega_m t})^* e^{-j3\omega_c t}}{j2} \quad (44)$$

$$V_{s3,upper3} = \frac{(B_{u,3} e^{j3\omega_m t}) e^{j3\omega_c t} - (B_{u,3} e^{j3\omega_m t})^* e^{-j3\omega_c t}}{j2} \quad (45)$$

$$V_{s3,lower3} = \frac{(B_{l,3} e^{-j3\omega_m t}) e^{j3\omega_c t} - (B_{l,3} e^{-j3\omega_m t})^* e^{-j3\omega_c t}}{j2} \quad (46)$$

Where $B_o, B_u, B_l, B_{u,2}, B_{l,2}, B_{u,3}, B_{l,3}$ are defined by Equations 47 - 53

$$B_o = J_0(\beta) \times \frac{4V_g}{\pi} H(j3\omega_c) \quad (47)$$

$$B_u = J_1(\beta) \times \frac{4V_g}{3\pi} H(j(3\omega_c + \omega_m)) \quad (48)$$

$$B_l = -J_1(\beta) \times \frac{4V_g}{3\pi} H(j(3\omega_c - \omega_m)) \quad (49)$$

$$B_{u,2} = J_2(\beta) \times \frac{4V_g}{3\pi} H(j(3\omega_c + 2\omega_m)) \quad (50)$$

$$B_{l,2} = -J_2(\beta) \times \frac{4V_g}{3\pi} H(j(3\omega_c - 2\omega_m)) \quad (51)$$

$$B_{u,3} = J_3(\beta) \times \frac{4V_g}{3\pi} H(j(3\omega_c + 3\omega_m)) \quad (52)$$

$$B_{l,3} = -J_3(\beta) \times \frac{4V_g}{3\pi} H(j(3\omega_c - 3\omega_m)) \quad (53)$$

The resonant tank circuit $H(s)$ is given by Figure 29 and the s-domain transfer function is given by Equation 54.

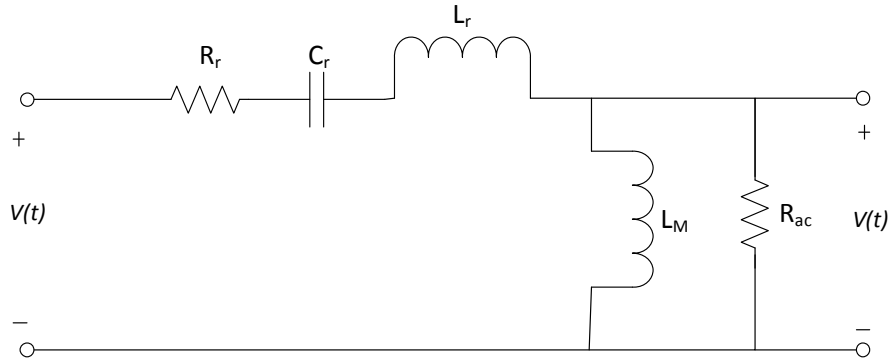


Figure 29: Tank filter circuit schematic with equivalent resistance R_{ac}

$$H(s) = \frac{s^2 C_r R_{ac} L_M}{s^3 L_r C_r L_M + s^2 (C_r R_{ac} L_M + L_M C_r R_r + L_r C_r R_{ac}) + s(L_M + R_r C_r R_{ac}) + R_{ac}} \quad (54)$$

In the above equations, the frequency domain variable s is taken such that $s = j\omega_m$, and $j\omega_c$ is the quiescent operating point. This is done in order to work in terms of the relative frequency, rather than the absolute frequency.

The individual mathematical representations of the fundamental, third and fifth harmonic voltage outputs from the resonant tank have now been determined. The total output voltage of the resonant tank is then the sum of the harmonic output equations. The complete output voltage equation can therefore be written as

$$v(t) = ||A|| \sin(\omega_c t + \angle A) + ||B|| \sin(3\omega_c t + \angle B) + ||C|| \sin(5\omega_c t + \angle C) \quad (55)$$

Continuing with the previous given example, the vector B is therefore defined as

$$B = B_o + B_u e^{j\omega_m t} + B_l e^{-j\omega_m t} + B_{u,2} e^{j2\omega_m t} + B_{l,2} e^{-j2\omega_m t} + B_{u,3} e^{j3\omega_m t} + B_{l,3} e^{-j3\omega_m t} \quad (56)$$

Equation 55 represents the output voltage as a sinusoid having time-varying amplitude and also time-varying phase.

Since the goal of this analysis is to determine the change in output voltage due to the effect of small variations to the switching frequency, the magnitude of Equation 55 must be evaluated. As was discussed, the effect of passing frequency signals through the resonant tank is the same as applying amplitude modulation (AM). Therefore, similar to AM analysis techniques, the envelope of the waveform should be extracted to study the change in the output voltage [33].

From AM analysis, it is known that the magnitude of the coefficients $\|A\|$, $\|B\|$, and $\|C\|$ contain the envelope of the signal. The square of the magnitude can firstly be determined by multiplying the vector with its complex conjugate. E.g. for B , the magnitude can be determined by

$$\|B\|^2 = BB^* \quad (57)$$

To make use of some mathematical simplifications, it is assumed that only the dominant DC components are relevant. If this is true, then the following approximation can be made.

$$\sqrt{1 + \xi} \approx 1 + \frac{1}{2}\xi \quad (58)$$

Thus, the magnitudes of A , B , and C are determined to be

$$\begin{aligned} \|A\| = & \|A_o\| + \|A_l\| \\ & + \frac{\|A_o A_l^* + A_u A_o^* + A_l A_{l,2}^* + A_{u,2} A_u^*\|}{\|A_o\|} \sin(\omega_m t + \angle(A_o A_l^* + A_u A_o^* + A_l A_{l,2}^* + A_{u,2} A_u^*)) \\ & + \frac{\|A_o A_{l,2}^* + A_u A_l^* + A_l A_{l,3}^* + A_{u,2} A_o^* + A_{u,3} A_u^*\|}{\|A_o\|} \sin(3\omega_m t + \angle(A_o A_{l,2}^* + A_u A_l^* + A_l A_{l,3}^* + A_{u,2} A_o^* + A_{u,3} A_u^*)) \\ & + \frac{\|A_o A_{l,3}^* + A_u A_{l,2}^* + A_{u,2} A_l^* + A_{u,3} A_o^*\|}{\|A_o\|} \sin(5\omega_m t + \angle(A_o A_{l,3}^* + A_u A_{l,2}^* + A_{u,2} A_l^* + A_{u,3} A_o^*)) \quad (59) \end{aligned}$$

$$\begin{aligned}
||B|| &= ||B_o|| + ||B_l|| \\
&+ \frac{||B_o B_l^* + B_u B_o^* + B_l B_{l,2}^* + B_{u,2} B_u^*||}{||B_o||} \sin(\omega_m t + \angle(B_o B_l^* + B_u B_o^* + B_l B_{l,2}^* + B_{u,2} B_u^*)) \\
&+ \frac{||B_o B_{l,2}^* + B_u B_l^* + B_l B_{l,3}^* + B_{u,2} B_o^* + B_{u,3} B_u^*||}{||B_o||} \sin(3\omega_m t + \angle(B_o B_{l,2}^* + B_u B_l^* + B_l B_{l,3}^* + B_{u,2} B_o^* + B_{u,3} B_u^*)) \\
&+ \frac{||B_o B_{l,3}^* + B_u B_{l,2}^* + B_{u,2} B_l^* + B_{u,3} B_o^*||}{||B_o||} \sin(5\omega_m t + \angle(B_o B_{l,3}^* + B_u B_{l,2}^* + B_{u,2} B_l^* + B_{u,3} B_o^*)) \quad (60)
\end{aligned}$$

$$\begin{aligned}
||C|| &= ||C_o|| + ||C_l|| \\
&+ \frac{||C_o C_l^* + C_u C_o^* + C_l C_{l,2}^* + C_{u,2} C_u^*||}{||C_o||} \sin(\omega_m t + \angle(C_o C_l^* + C_u C_o^* + C_l C_{l,2}^* + C_{u,2} C_u^*)) \\
&+ \frac{||C_o C_{l,2}^* + C_u C_l^* + C_l C_{l,3}^* + C_{u,2} C_o^* + C_{u,3} C_u^*||}{||C_o||} \sin(3\omega_m t + \angle(C_o C_{l,2}^* + C_u C_l^* + C_l C_{l,3}^* + C_{u,2} C_o^* + C_{u,3} C_u^*)) \\
&+ \frac{||C_o C_{l,3}^* + C_u C_{l,2}^* + C_{u,2} C_l^* + C_{u,3} C_o^*||}{||C_o||} \sin(5\omega_m t + \angle(C_o C_{l,3}^* + C_u C_{l,2}^* + C_{u,2} C_l^* + C_{u,3} C_o^*)) \quad (61)
\end{aligned}$$

In Equations 59, 60, and 61, it is shown that each harmonic component has a DC and a small signal cosine term. It is known that the envelope function is represented by the amplitude of the small signal term, and this is the value of output voltage that is to be observed in the control-to-output transfer function.

Therefore, to get the transfer function $P(s) = \frac{V_o}{f}$, the magnitude of the envelope voltage expression is divided by the small signal variation in frequency represented by $\frac{\Delta\omega}{2\pi}$, as defined by Equation 22.

5.2.5 Results of Frequency and Amplitude Modulation

Figure 30 shows the frequency response of each harmonic component and shows the contribution of each harmonic after being filtered by the resonant tank circuit. The results of Figure 30 confirm the third and fifth harmonic components have significant contribution to the transfer function, and therefore it has been shown that they may not be neglected in analysis.

The result of the summation of the fundamental, third and fifth harmonic components is also shown in Figure 30.

For comparison, Figure 31 is a plot of the fundamental harmonic component and shows the effect of including and not including the sideband frequencies in the derivation model. From the results of Figure 31, it can be seen that the sideband frequencies have a significant effect on the resulting magnitude plot.

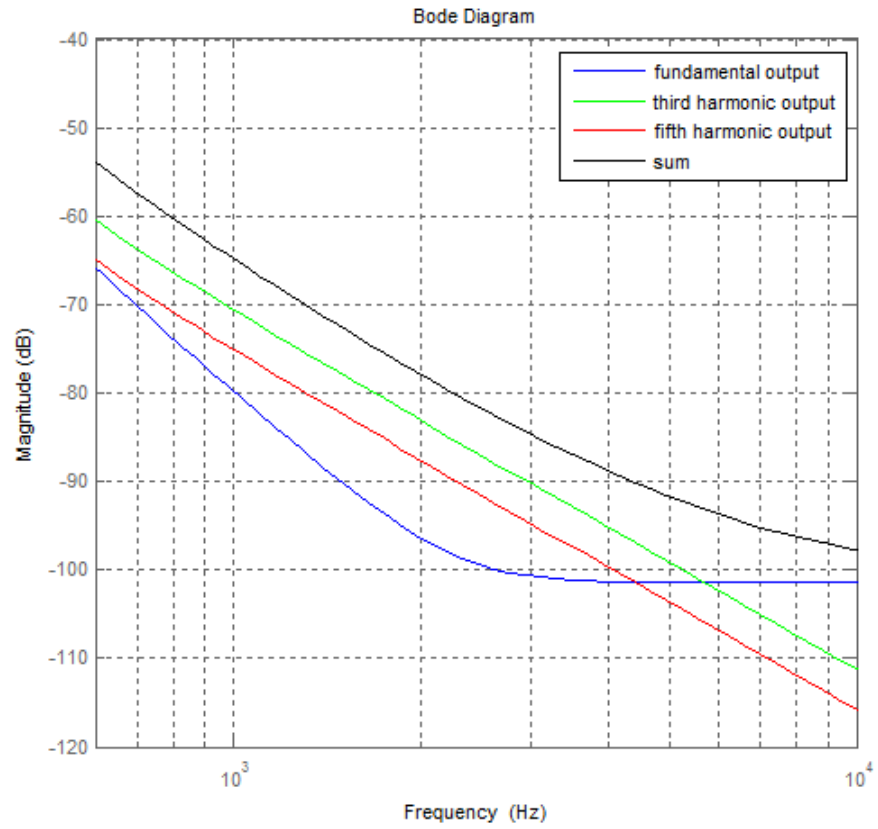


Figure 30: Comparison of the significance between fundamental, third and fifth harmonics

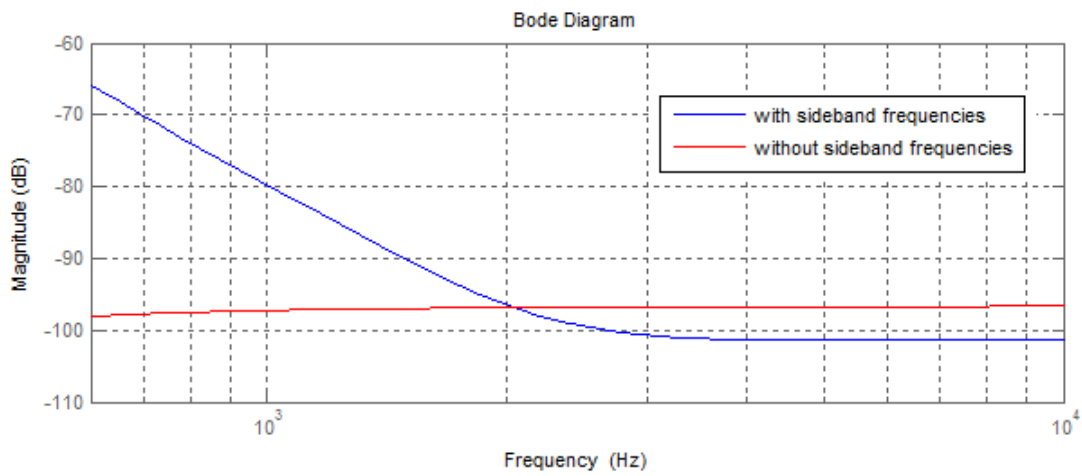


Figure 31: Comparison of the fundamental component, with and without sideband frequencies

5.2.6 Isolation Transformer and Rectification Stage

The next stage of the LLC resonant topology is the high frequency isolation transformer, located after the resonant stage. To model the effect of the transformer on the control-to-output transfer function, the transformer turns ratio can be multiplied to the magnitude of Equation 55 in order to get an equation of the voltage seen on the secondary side of the converter.

$$v_{secondary}(t) = \frac{N_1}{N_2} \times v(t) \quad (62)$$

The frequency response data of Figure 18 shows that a pole-zero combination appears at high frequencies. It was determined that the cause of the zero is a result of the output capacitor equivalent series resistance, as well as the presence of a right hand plane zeros (RHPZ). In [36], it is stated that the RHPZ is a result of the inductor current not being able to instantaneously change, and is a function of the inductance and load [37].

The ESR zero is located at a fixed frequency, and is given by Equation 63.

$$\omega_{esr} = \frac{1}{C_o R_c} \quad (63)$$

The ESR and RHPZ zeros are compensated by high frequency poles which were determined to be contributed by system delays [38]. A system delay in the s-domain can be given by

$$H_{delay}(s) = e^{-sT} \quad (64)$$

To evaluate Equation 64, the third order Padé approximation is used and the transfer function of the high frequency pole is given by Equation 65 [39].

$$e^{-sT} \approx \frac{60 - 24sT + 3(sT)^2}{60 + 36sT + 9(sT)^2 + (sT)^3} \quad (65)$$

By combining all of the above effects presented with the results of Figure 30, the analysis finally gives the magnitude plot of the derivation model of the control-to-output transfer function. The results of the analysis can be compared to the frequency response data of Chapter 4 and are shown in Figure 32.

5.2.7 Results of Analysis of the Derivation Model

Figure 32 compares the results of the derivation model and the frequency response data of the prototype model. From the results, it can be seen that the derivation model is a good approximation of the frequency response data, and therefore confirms the proposed model is adequate for modelling the small signal control-to-output transfer function. Therefore, it has been shown that by including

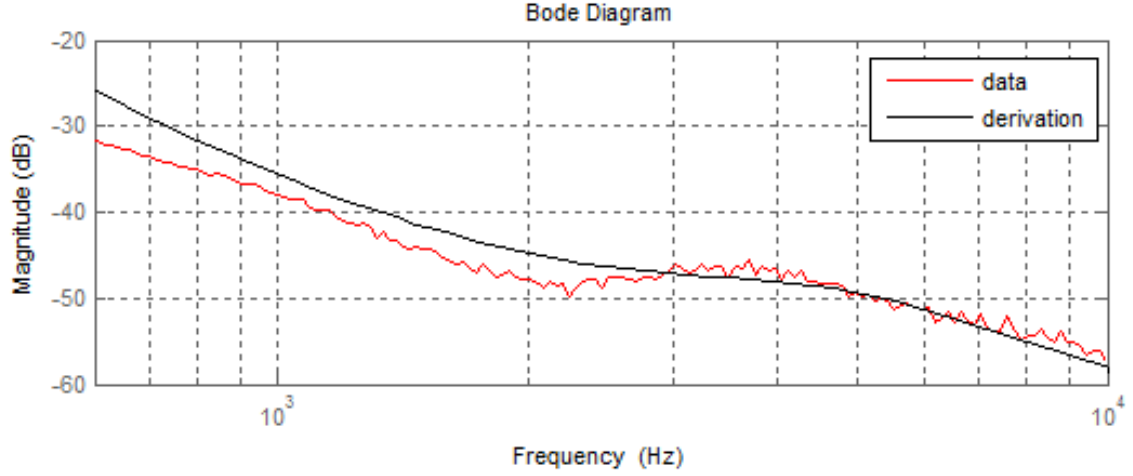


Figure 32: Comparison of prototype frequency response data and derivation model (magnitude)

harmonics up to the fifth harmonic, as well as sideband frequencies in the derivation model, a reasonably accurate model of the small signal control-to-output transfer function can be achieved.

From Figure 32, it is observed that at the lower frequencies, the error is largest, and there is approximately a maximum of 5 dB difference between the frequency response data and the derivation model. This non-conformity can be attributed to have not included enough of the sideband frequencies in the model.

As was discussed in Section 5.2.3, the derivation model only considers the sideband frequencies that appear under the condition $\omega_m = 1000\pi$ rad/s. The equivalent value of this ω_m in frequency is at 500 Hz, and from Figure 32, it can be seen that this is approximately the point at which the discrepancies appear. Therefore, if the chosen value of ω_m was smaller, more sideband frequencies would have been added to the model, and the accuracy of the derivation model would improve for the low frequency region.

The importance of the sideband frequencies is further shown in Figure 32, such that for frequencies greater than 2 kHz, the derivation model gives a very close approximation of the magnitude response of the bench prototype model.

5.2.8 Phase Response of Control-to-Output Transfer Function

To gain an understanding of the phase response of the control-to-output transfer function, the asymptotic Bode tracing technique of [40] can be applied to the magnitude response. This method approximates the s-domain transfer function of frequency response plots by using knowledge of the behaviors of simple poles and zeros.

$$|H(s)| = k \frac{\prod_{i=1}^m |(s - z_i)|}{\prod_{i=1}^n |(s - p_i)|} \quad (66)$$

$$\angle H(s) = \sum_{i=1}^m \angle(s - z_i) - \sum_{i=1}^n \angle(s - p_i) \quad (67)$$

By extracting an approximate s-domain transfer function equation of the magnitude response, the corresponding phase response can be obtained. The accuracy of the plot can be increased simply by increasing the number of poles and zeros used to model the magnitude response.

The curve fit result is shown in Figure 33 and is compared to the frequency response phase data.

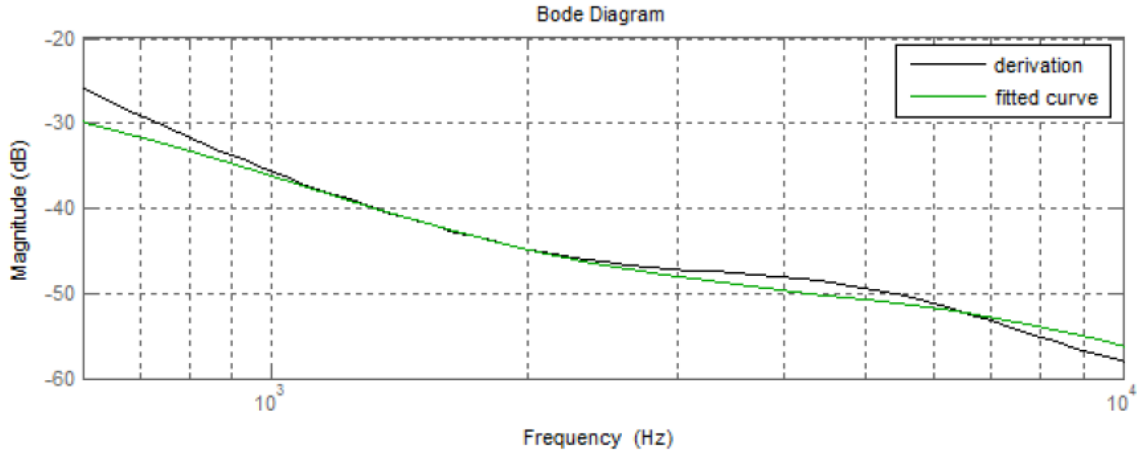


Figure 33: Comparison of derivation model and curve fit model (magnitude)

Figure 33 shows a reasonable curve fitting of the derivation model frequency response. As previously stated, the accuracy of the curve fit can be adjusted by increasing the number of poles and zeros used during the curve fitting process.

There are several alternative methods in which a curve fit of the frequency response can be obtained. However, compared to asymptotic Bode tracing, many of the analytical methods presented in literature such as [41] [42], are cumbersome and unmanageable for normal use, and methods that use software tools are costly to acquire and offer little to no flexibility in terms of pole/zero placement [30].

Figure 34 compares the results of the phase plot from the derivation model and is compared with the frequency response data of Chapter 4. The results appear to be a good quality approximation of the obtained data. However, it can be noted that the curve fit model presents a more pessimistic view of the phase response, and was unable to capture phase lead characteristic between 2 and 4 kHz.

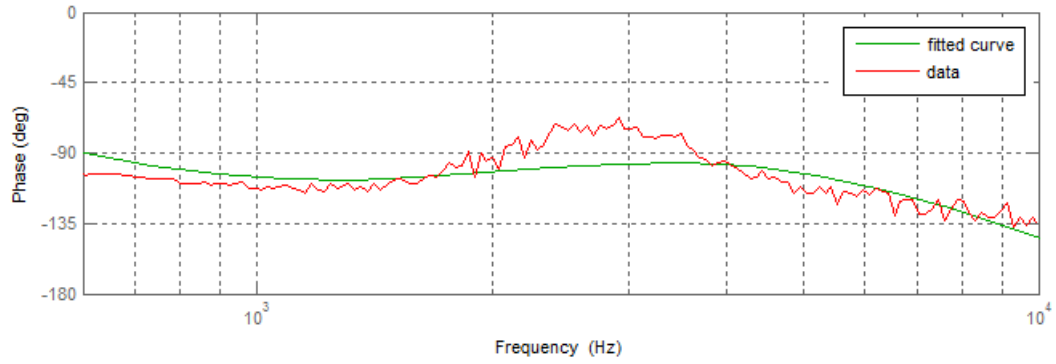


Figure 34: Comparison of prototype frequency response data and curve fit model (phase)

5.3 Verification of Derivation Model in PSIM[®]

To verify that the derivation model can be used as an approximation of the control-to-output transfer function, a compensator based on the derivation model results was designed in MATLAB[®]. The results are shown in Figures 35 - 38, and are summarized in Table 2.

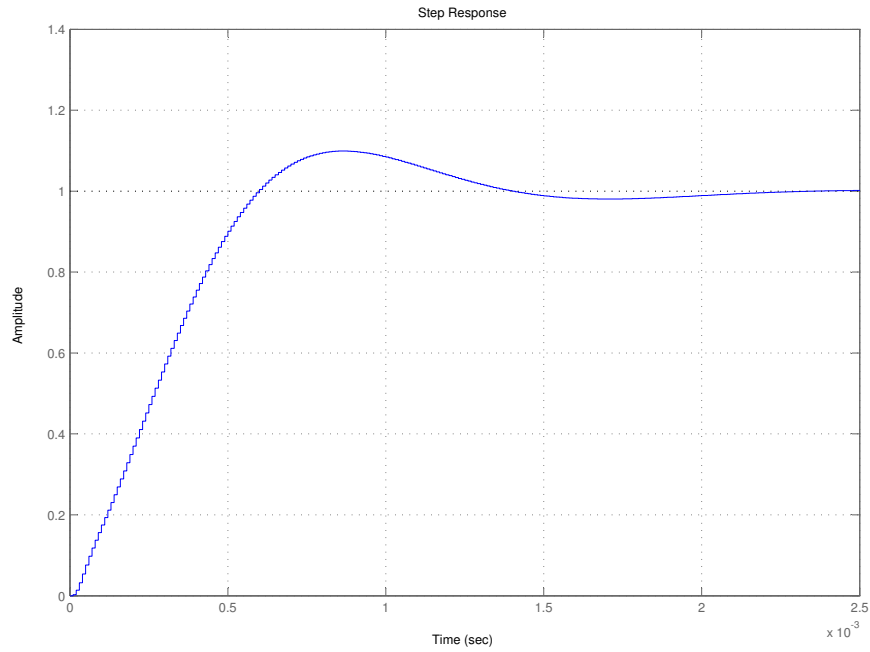


Figure 35: MATLAB[®] step response of closed-loop system using derivation model

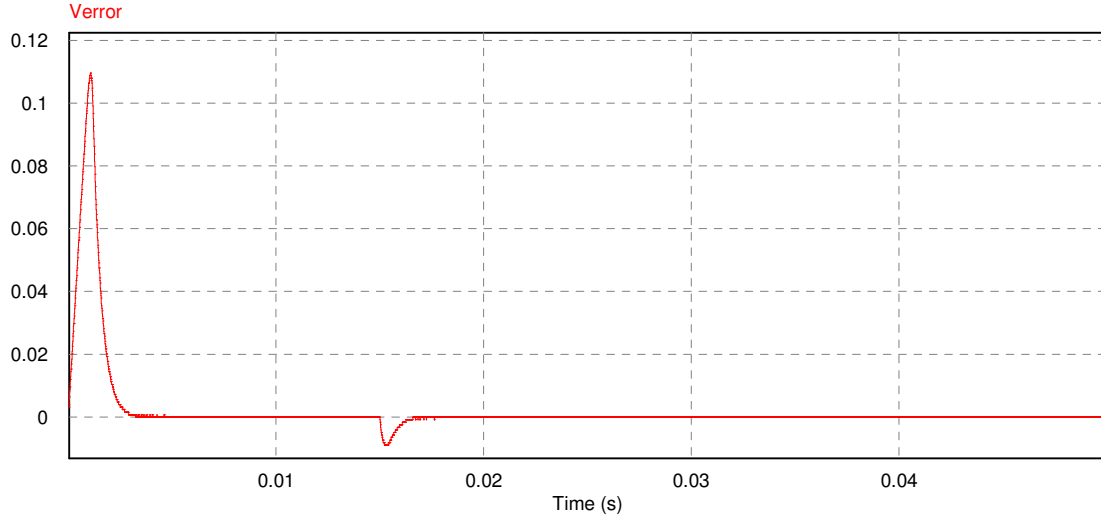


Figure 36: Error voltage of derivation model

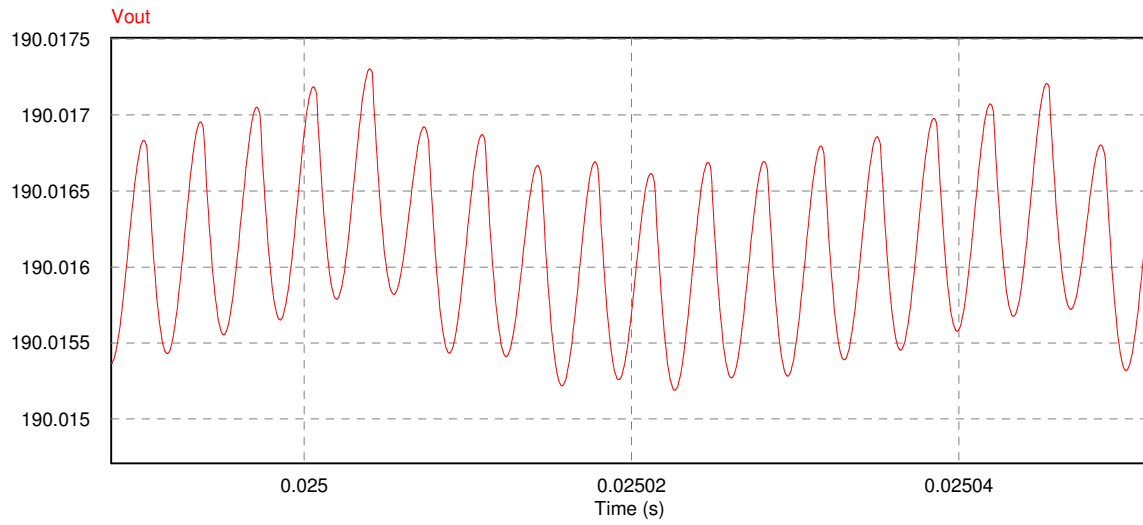


Figure 37: Output voltage ripple of derivation model

The results of the digital negative feedback control system designed by using the derivation model are summarized in Table 2. It was found that the results of Table 2 are comparable to those of Table 1 found in Chapter 4. Therefore, it can be concluded that the derivation model can be used for digital compensator design, and is able to produce similar results to a compensator designed based on physical prototype data.

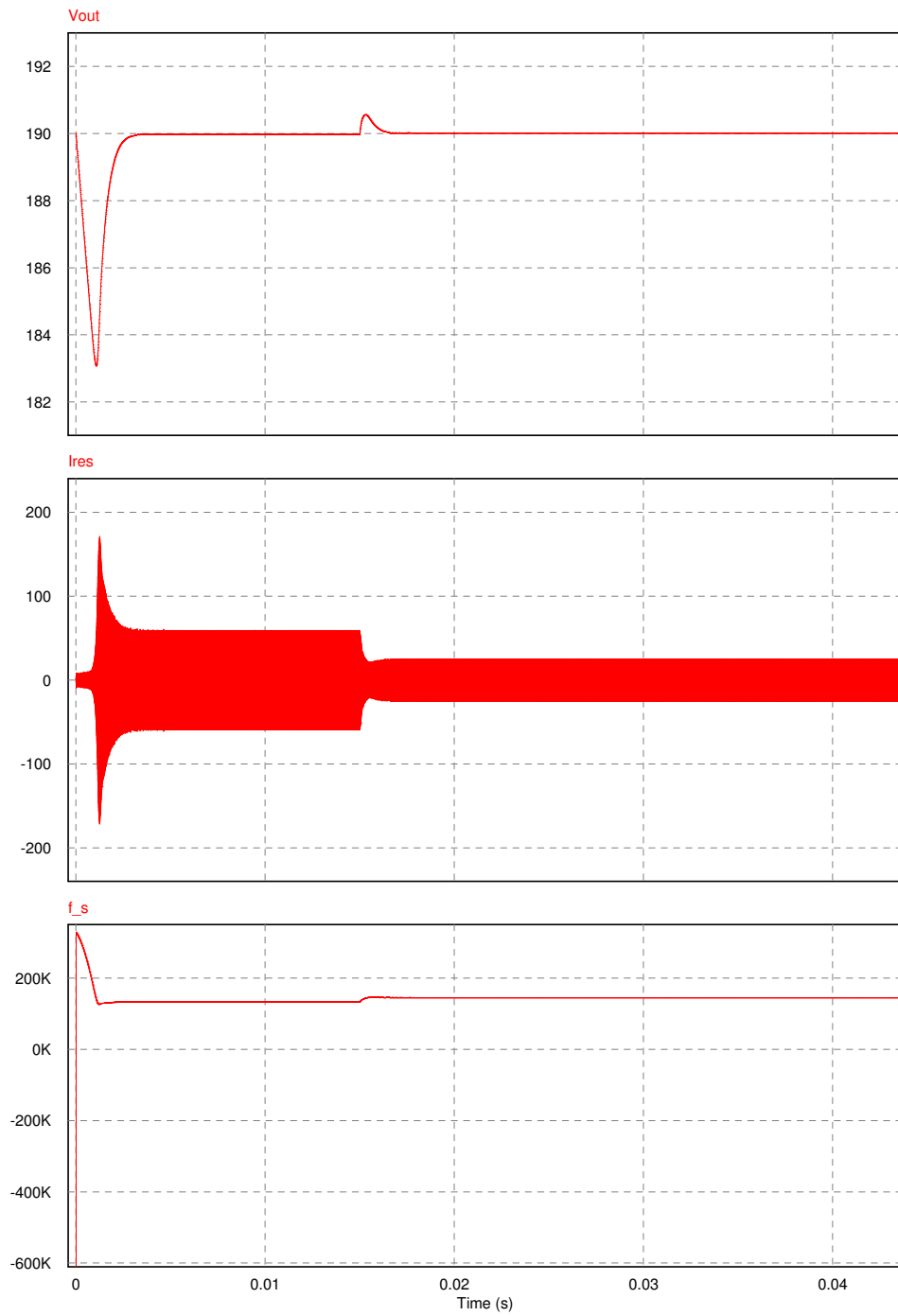


Figure 38: PSIM® closed-loop response to step load change using prototype model

Output voltage value:	190 V
Steady-state error:	0 V
Output voltage ripple	1.5 mV
% overshoot:	10%
Rise-time:	0.9 ms
Settling-time:	2 ms

Table 2: Results of derivation model

The merit of these results is the confirmation that the small signal control-to-output transfer function obtained by the derivation model can also be used to determine a digital compensator in lieu of using prototype frequency response data. The first advantage of the derivation model method is that only the circuit parameters of the proposed LLC resonant converter are required, and no physical prototype model is needed to obtain the frequency response data. Secondly, compared to computer simulation software which can also be used to obtain the plant transfer function, the derivation model requires significantly less computational power, and is considerably faster in terms of simulation run-time.

6 Conclusions and Future Work

6.1 Summary

In this thesis, the LLC resonant converter topology and the variable frequency control method for output voltage regulation was discussed in detail.

In Chapter 2, it was determined that the LLC resonant converter is an excellent choice for a power electronic converter topology to be used in isolated DC-DC conversion applications. The LLC resonant converter was found to feature high efficiency, high power density, and the ability to operate over a wide range of loading conditions. The LLC resonant converter also has many other advantageous features including low electromagnetic interference, and soft-switching capabilities.

Chapter 3 discusses the application of a controller to the LLC resonant converter. It was determined that the preferred control method under nominal loading conditions is variable frequency control, a method which varies the switching frequency of the converter to regulate the output voltage. The 2-pole-2-zero compensator was introduced as a possible suitor for a digital control system, as it can be easily implemented within digital signal processors by using difference equations. The stability of continuous and discrete-time control systems was also discussed and the application of Bode diagrams and Nyquist plots for control system design was explored.

It was then shown in Chapter 4 that by using a combination of laboratory bench measurements, and computer simulation, that a digital compensator could be designed to very tightly regulate the output voltage. An algorithm was then presented to implement the voltage control loop in a digital signal processor.

In Chapter 5, a novel derivation of the small signal control-to-output transfer function was completed. The model includes the use of the fundamental, third and fifth harmonics, and showed that the higher order harmonics have a significant contribution to the overall transfer function, and it should be necessary to include them to capture the true dynamics of the control-to-output transfer function. The new model also includes higher order sideband frequencies and it was confirmed that the higher order sideband frequencies are required for modelling the converter for the case(s) where the magnitude of the modulation index β does not meet the condition $|\beta| < 1$.

It was then verified that the small signal control-to-output transfer function developed in the derivation model could be used to design a digital compensator for a digital negative feedback control system. The simulation results show that an acceptable closed-loop step response and output voltage regulation was achieved, and had comparable results to the results of Chapter 4.

Finally, it was concluded that the results of Chapter 5 were comparable to the results of Chapter 4 and that the small signal control-to-output transfer function could be obtained using the derivation model. The advantages of using the derivation model are reduced computational complexity and the diminished requirement for a physical prototype model.

6.2 Future Work

There are several areas which can be explored further to improve the modelling of the LLC resonant converter control-to-output transfer function.

Firstly, development of the model for the low frequency range can be investigated, and can be achieved by decreasing the value of ω_m , and therefore, introducing the case where modulation index β is large. To calculate large values of β , a different method to calculate and obtain the Bessel function coefficient $J_n(\beta)$ may be required.

Secondly, a more in depth method to describe the rectifier model is also needed. As there are certain loading conditions which cause the LLC resonant converter to go into discontinuous conduction mode, the linearization of the rectifier circuit may not be valid for all scenarios.

Thirdly, another topic of interest would be to determine a practical method in which synchronous rectification can be achieved. In addition to an increase in the efficiency of the converter, there is also potential of having bidirectional power flow between the input and output. In the case where a battery is used to provide DC power at the input, this means the battery could also be charged by the load without any additional conversion processes.

Fourthly, it was also observed that there was a significant effect on the control-to-output transfer function from the output capacitance and its equivalent series resistance. Therefore, a self-tuning controller has potential to be of great value for the design of controllers for the LLC resonant converter. It may be able to offset errors in the modelling process that are caused by the tolerances, the effects of aging capacitance, or the variation in capacitance from operation in environments with non-ideal temperatures.

Lastly, there have also been several improvements in switching device technology since the beginning of this work. Silicon carbide-based transistors and diodes have been shown many significant advantages including lower conduction losses, higher frequency operation, as well as higher operable temperatures.

References

- [1] D. Becker and B. Sonnenberg, “Dc microgrids in buildings and data centers,” in *Telecommunications Energy Conference (INTELEC), 2011 IEEE 33rd International*, 2011.
- [2] B. Mammano, “Resonant mode converter topologies,” pp. 1–2, 2001. Texas Instruments application note.
- [3] F. Canales, P. Barbosa, and F. C. Lee, “A wide input voltage and load output variations fixed-frequency zvs dc/dc llc resonant converter for high-power applications,” in *Industry Applications Conference, 37th IAS Annual Meeting*, 2002.
- [4] G. Pledl, M. Tauer, and D. Buecherl, “Theory of operation, design procedure and simulation of a bidirectional llc resonant converter for vehicular applications,” in *Vehicle Power and Propulsion Conference (VPPC), 2010 IEEE*, 2010.
- [5] D. J. Tschirhart and P. K. Jain, “Digital control of resonant converters at ultra high frequency,” in *Telecommunications Energy Conference (INTELEC), 32nd International*, 2010.
- [6] R. W. Erickson and D. Maksimovic, *Fundamentals of Power Electronics*. Springer; 2nd edition, 2001.
- [7] B. Yang, *Topology investigation of front end DC/DC converter for distributed power system*. PhD thesis, Virginia Polytechnic Institute and State University, 2003.
- [8] B. Lu, W. Liu, Y. Liang, F. C. Lee, and J. D. van Wyk, “Optimal design methodology for llc resonant converter,” in *Applied Power Electronics Conference and Exposition, 2006. APEC '06. Twenty-First Annual IEEE*, 2006.
- [9] R. Locher, “Introduction to power mosfets and their applications,” p. 1, 1998.
- [10] Y.-F. Liu and W. Eberle, “Recent developments in switching mode power supply technologies,” *IEEE Canadian Review*, vol. 61, pp. 9–13, 2009.
- [11] D. Fu, *Topology Investigation and System Optimization of Resonant Converters*. PhD thesis, Virginia Polytechnic Institute and State University, 2010.
- [12] H. Choi, “Analysis and design of llc resonant converter with integrated transformer,” in *Applied Power Electronics Conference, APEC 2007 - Twenty Second Annual IEEE*, 2007.
- [13] D. Fu, Y. Liu, F. C. Lee, and M. Xu, “A novel driving scheme for synchronous rectifiers in llc resonant converters,” *Power Electronics, IEEE Transactions on*, vol. 24, pp. 1321–1329, 2009.

- [14] D. Wang, L. Jia, Y.-F. Liu, and P. Sen, "An improved driving method for synchronous rectifier using drain-source voltage sensing," in *Applied Power Electronics Conference and Exposition (APEC), 2011 Twenty-Sixth Annual IEEE*, 2011.
- [15] Y. Liu, "High efficiency optimization of llc resonant converter for wide load range," Master's thesis, Virginia Polytechnic Institute and State University, 2007.
- [16] Y. Ye, C. Yan, J. Zeng, and J. Ying, "A novel light load solution for llc series resonant converter," in *Telecommunications Energy Conference, 2007. INTELEC 2007. 29th International*, 2007.
- [17] W.-J. Lee, S.-W. Choi, C.-E. Kim, and G.-W. Moon, "A new pwm-controlled quasi-resonant converter for a high efficiency pdp sustaining power module," *Power Electronics, IEEE Transactions on*, vol. 23, pp. 1782–1790, 2008.
- [18] R. Poley, "Digital control theory seminar; student manual." Texas Instruments, 2012.
- [19] G. F. Franklin, J. D. Powell, and M. L. Workman, *Digital Control of Dynamic Systems*. Addison-Wesley, 1998.
- [20] B. Akin and D. Chang, "Optimal digital power control using llc resonant converters," April 2012.
- [21] M. Gopal, *Control Systems: Principles and Design*. Tata McGraw-Hill Publishing Company, 2008.
- [22] S. Engelberg, *A Mathematical Introduction to Control Theory*. Imperial College Press, 2005.
- [23] G. F. Franklin, J. D. Powell, and A. Emami-Naeini, *Feedback Control of Dynamic Systems*. Addison-Wesley Long Man Publishing Co., 1993.
- [24] R. Poley, "Control theory seminar; student manual." Texas Instruments, 2012.
- [25] S. M. Shinnars, *Modern Control System Theory and Design*. John Wiley & Sons, 1998.
- [26] MATLAB, *version 7.11.0.584 (R2010b)*. Natick, Massachusetts: The MathWorks Inc., 2010.
- [27] Powersim, *PSIM User Manual*. www.powersimtech.com.
- [28] N. Macia, *Modeling and Control of Dynamic Systems*. Thomson Delmar Learning, 2005.
- [29] S. Chon, "What it takes to do efficient and cost-effective real-time control with a single micro-controller: The c2000 advantage," p. 3, January 2011.

- [30] P. Spanik, P. Drgona, and M. Frivaldsky, "Simulation based method for mathematical model design of llc power converter,"
- [31] H. Huang, "Feedback loop design of an llc resonant power converter," *Texas Instruments Application Report*, 2010.
- [32] J. Jang, M. Joung, S. Choi, Y. Choi, and B. Choi, "Current mode control for llc series resonant dc-to-ac converters," in *Applied Power Electronics Conference and Exposition (APEC), 2011 Twenty-Sixth Annual IEEE*, 2011.
- [33] T. G. Thomas and S. C. Sekhar, *Communication Theory*. Tata McGraw-Hill Publishing Company, 2006.
- [34] M. Abramowitz and I. A. Stegun, *Handbook of Mathematical Functions With Formulas, Graphs, and Mathematical Tables*. National Bureau of Standards Applied Mathematics Series, December 1972.
- [35] R. W. Erickson, "Fm/am modeling of the envelope transfer function." ECEN 5817 course notes.
- [36] C. P. Basso, *Switch-Mode Power Supply SPICE Cookbook*. McGraw-Hill Prof Med/Tech, 2001.
- [37] R. Zaitsev, "Voltage mode boost converter small signal control loop analysis using the tps61030," *Texas Instruments Application Report*, pp. 2–8, 2009.
- [38] R. Petkov and G. Angelov, "Current mode control of frequency controlled resonant converters," in *Telecommunications Energy Conference, 1998. INTELEC. Twentieth International*, 1998.
- [39] M. Vajta, "Some remarks on pade approximations," in *3rd TEMPUS-INTCOM Symposium*, 2000.
- [40] J. Marti, "Wave propagation in frequency dependent lines: The fd-line model," 2004. EECE 560 course notes.
- [41] W. S. Cleveland, S. J. Devlin, and E. Grosse, "Regression by local fitting: Methods, properties, and computational algorithms," *Journal Of Econometrics*, vol. 37, pp. 87–114, 1988.
- [42] G. Ferreres and J. Biannic, "Frequency domain curve fitting: a generalized approach," tech. rep., ONERA/DCSD: Systems Control and Flight Dynamics Department, 2001.

Appendices

Appendix A: Observation of Stability in Continuous and Discrete-time domains

A1: Continuous-time domain

To determine the stability and the dynamic characteristics of the closed loop feedback system of Figure 14, the transfer function of Figure 14 can be described by Equation A-1. Assuming that the actuator has a gain equal to 1,

$$T(s) = \frac{G(s)P(s)}{1 + G(s)P(s)} \quad (\text{A-1})$$

In the continuous-time domain, the stability of the feedback system is observed on the s-domain plane. The stability can be determined by evaluating the denominator of Equation A-1, also known as the characteristic equation. Solving for the roots of the characteristic equation gives the poles of the system, which are indicators of the system's stability.

A system that contains only poles on the left hand side of the $j\omega$ axis of the s-domain plane are considered to be stable, while systems with poles on the right hand side of the $j\omega$ axis are unstable. Marginally stable systems have poles on the $j\omega$ axis.

A2: Discrete-time domain

In the discrete-time domain, the stability of the feedback system is observed with respect to the z-domain unit circle. Stable systems have all poles located inside of the unit circle, while unstable systems have poles located outside of the unit circle. Finally, marginally stable systems have poles located on the unit circle.

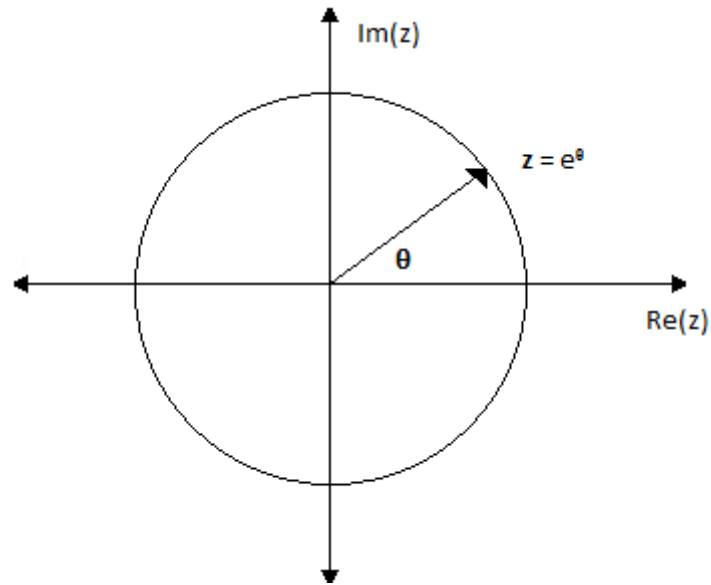


Figure A-1: Unit circle in the z-domain

Appendix B: PSIM® simulation schematics

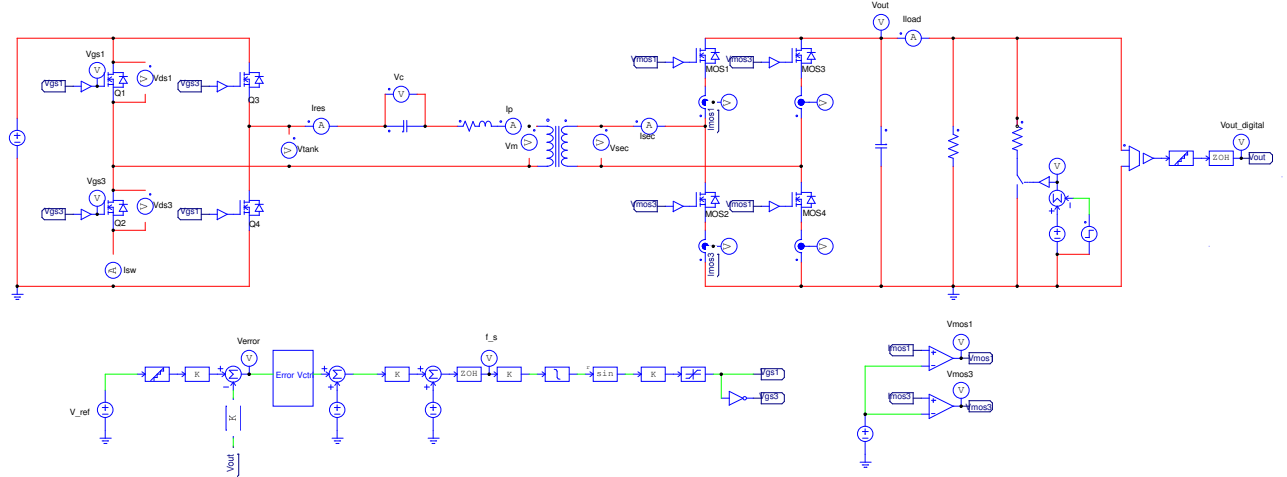


Figure B-1: PSIM® closed loop circuit schematic of LLC resonant converter

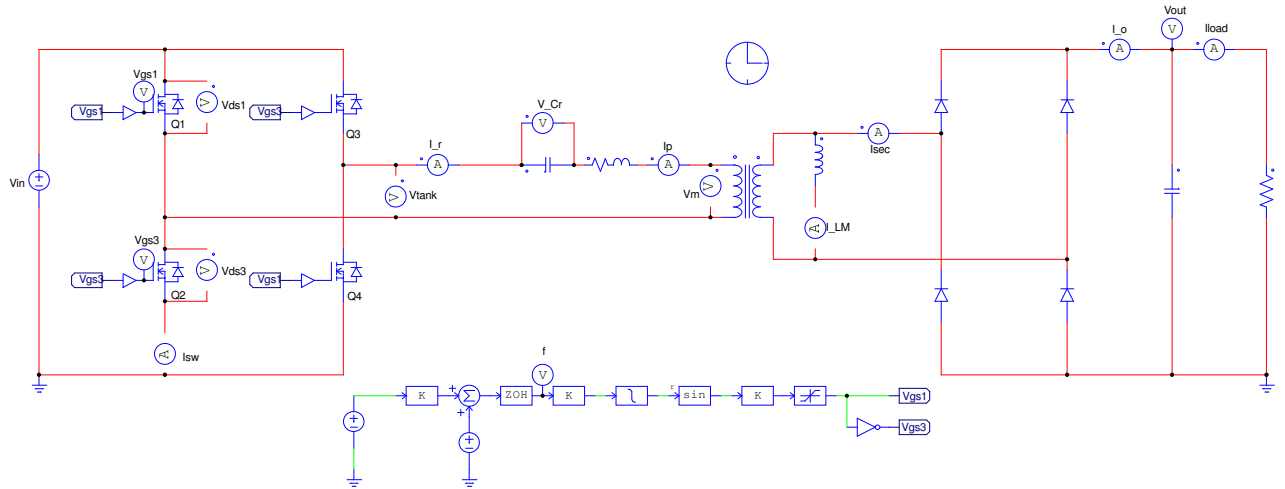


Figure B-2: PSIM® open loop circuit schematic of LLC resonant converter

Appendix C: MATLAB®derivation model code

```
1 clear all
2 close all
3 clc
4
5 Vg = 48;
6 Kvco = 32779;
7 Tratio = 15/4;
8
9 delta_w = 2*pi*(Kvco)*0.02;
10
11 Lm = (80e-6)*((4/15)^2);
12 Lr = (10e-6)/((15/4)^2);
13 Cr = 9*270e-9;
14 R = 1;
15 Rr = R;
16 Ro = 170/4.6;
17 Rac = ((8*Tratio^2)/pi^2)*Ro;
18
19 res_freq = 1/(sqrt(Lr*Cr)*2*pi)
20 w_so = 2*pi*res_freq;
21
22 V_s1 = (4/pi)*Vg;
23 V_s3 = (4/(3*pi))*Vg;
24 V_s5 = (4/(5*pi))*Vg;
25
26 Rc = 0.159;
27 C = 470e-6;
28 ESRzero = tf([C*Rc 1],[1]);
29 [mag_ESRzero phase_ESRzero] = bode(ESRzero,logspace(1,6,200));
30 mag_ESRzero = squeeze(mag_ESRzero);
31 phase_ESRzero = squeeze(phase_ESRzero);
32
33 fz = 3100;
34 RHPzero = tf([-1/(2*pi*fz) 1],[1]);
35 [mag_RHPzero phase_RHPzero] = bode(RHPzero,logspace(1,6,200));
36 mag_RHPzero = squeeze(mag_RHPzero);
37 phase_RHPzero = squeeze(phase_RHPzero);
38
39 T = 1/8000;
40 ZOHpole = tf([3*T^2 -24*T 60],[T^3 9*T^2 36*T 60]);
41 [mag_ZOHpole phase_ZOHpole] = bode(ZOHpole,logspace(1,6,200));
42 mag_ZOHpole = squeeze(mag_ZOHpole);
43 phase_ZOHpole = squeeze(phase_ZOHpole);
44
45 %%%%%%%%%fundamental frequency
```

```

46 a = Cr*Rac*Lm;
47 b = Lr*Cr*Lm;
48 c = (Cr*Rac*Lm)+(Lm*Cr*Rr)+(Lr*Cr*Rac);
49 d = Lm+(Rr*Cr*Rac);
50 e = Rac;
51
52 %with Rload
53 H_jwso = tf([a*(i*w_so)^2],[b*(i*w_so)^3+c*(i*w_so)^2+d*(i*w_so)+e]);
54 H_jwsoConj = tf([a*(-i*w_so)^2],[b*(-i*w_so)^3+c*(-i*w_so)^2+d*(-i*w_so)+e]);
55
56 %with Rload
57 H_jwsoPluswsm = tf([a*a*2*i*w_so-a*w_so^2],[b*(b*3*i*w_so+c)*(-b*3*w_so^2+c*2*i*w_so
+d)*(e-c*w_so^2-b*i*w_so^3+d*i*w_so)]);
58 H_jwsoPluswsmConj = tf([a*a*2*i*w_so-a*w_so^2],[-b*(-b*3*i*w_so+c)*(b*3*w_so^2+c*2*i
*w_so-d)*(b*i*w_so^3-c*w_so^2-d*i*w_so+e)]);
59
60 %with Rload
61 H_jwsoMinuswsm = tf([a*-2*i*w_so*a-a*w_so^2],[-b*(b*3*i*w_so+c)*(b*3*w_so^2-c*2*i*
w_so-d)*(e-b*j*w_so^3-c*w_so^2+d*i*w_so)]);
62 H_jwsoMinuswsmConj = tf([a*-2*i*w_so*a-a*w_so^2],[-b*(-b*3*i*w_so+c)*(-b*3*w_so^2-c
*2*i*w_so+d)*(e-c*w_so^2+b*i*w_so^3-d*i*w_so)]);
63
64 %with Rload
65 H_jwsoPlus2wsm = tf([4*a*4*a*i*w_so-a*w_so^2],[8*b*(12*b*i*w_so+4*c)*(-b*6*w_so^2+4*
i*c*w_so+2*d)*(e+d*i*w_so-b*i*w_so^3-c*w_so^2)]);
66 H_jwsoPlus2wsmConj = tf([4*a*4*a*i*w_so-a*w_so^2],[-8*b*(-12*b*i*w_so+4*c)*(b*6*w_so
^2+4*i*w_so*c-2*d)*(b*i*w_so^3-c*w_so^2-d*i*w_so+e)]);
67
68 %with Rload
69 H_jwsoMinus2wsm = tf([4*a*-4*a*i*w_so-a*w_so^2],[-8*b*(12*b*i*w_so+4*c)*(6*b*w_so
^2-4*c*i*w_so-2*d)*(e+d*i*w_so-b*j*w_so^3-c*w_so^2)]);
70 H_jwsoMinus2wsmConj = tf([4*a*-4*a*i*w_so-a*w_so^2],[8*b*(-12*b*i*w_so+4*c)*(-6*b*
w_so^2-4*c*i*w_so+2*d)*(e-i*d*w_so-c*w_so^2+b*i*w_so^3)]);
71
72 %with Rload
73 H_jwsoPlus3wsm = tf([9*a*6*a*i*w_so-a*w_so^2],[27*b*(27*b*i*w_so+9*c)*(-9*b*w_so
^2+6*c*i*w_so+3*d)*(e+d*i*w_so-c*w_so^2-b*i*w_so^3)]);
74 H_jwsoPlus3wsmConj = tf([9*a*6*a*i*w_so-a*w_so^2],[-27*b*(-27*b*i*w_so+9*c)*(9*b*
w_so^2+6*c*i*w_so-3*d)*(e-i*d*w_so-c*w_so^2+b*i*w_so^3)]);
75
76 %with Rload
77 H_jwsoMinus3wsm = tf([9*a*-6*a*i*w_so-a*w_so^2],[-27*b*(27*b*i*w_so+9*c)*(9*b*w_so
^2-6*c*i*w_so-3*d)*(e+d*i*w_so-c*w_so^2-b*i*w_so^3)]);
78 H_jwsoMinus3wsmConj = tf([9*a*-6*a*i*w_so-a*w_so^2],[27*b*(-27*b*i*w_so+9*c)*(-9*b*
w_so^2-6*c*i*w_so+3*d)*(e-d*i*w_so-c*w_so^2+b*i*w_so^3)]);
79
80 beta = tf([delta_w],[-1*i_0]);

```

```

81 [mag_beta phase_beta wout] = bode(beta, logspace(1,6,200));
82 mag_beta = squeeze(mag_beta);
83 phase_beta = squeeze(phase_beta);
84
85 %fundamental, sideband 0
86 alpha = 0;
87 J0_1 = besselj(alpha, mag_beta);
88
89 [mag_H_jwso phase_H_jwso] = bode(H_jwso, logspace(1,6,200));
90 mag_H_jwso = squeeze(mag_H_jwso);
91 phase_H_jwso = squeeze(phase_H_jwso);
92
93 [mag_H_jwsoConj phase_H_jwsoConj] = bode(H_jwsoConj, logspace(1,6,200));
94 mag_H_jwsoConj = squeeze(mag_H_jwsoConj);
95 phase_H_jwsoConj = squeeze(phase_H_jwsoConj);
96
97 Ao_mag = V_s1*J0_1.*mag_H_jwso;
98 AoConj_mag = V_s1*J0_1.*mag_H_jwsoConj;
99
100 %fundamental sideband 1
101 alpha1_1 = 1;
102 J1_1 = besselj(alpha1_1, mag_beta);
103
104 %plus
105 [mag_H_jwsoPluswm phase_H_jwsoPluswm] = bode(H_jwsoPluswm, logspace(1,6,200));
106 mag_H_jwsoPluswm = squeeze(mag_H_jwsoPluswm);
107 phase_H_jwsoPluswm = squeeze(phase_H_jwsoPluswm);
108
109 [mag_H_jwsoPluswmConj phase_H_jwsoPluswmConj] = bode(H_jwsoPluswmConj, logspace
    (1,6,200));
110 mag_H_jwsoPluswmConj = squeeze(mag_H_jwsoPluswmConj);
111 phase_H_jwsoPluswmConj = squeeze(phase_H_jwsoPluswmConj);
112
113 Au_mag = V_s1*J1_1.*mag_H_jwsoPluswm;
114 AuConj_mag = V_s1*J1_1.*mag_H_jwsoPluswmConj;
115
116 %minus
117 [mag_H_jwsoMinuswm phase_H_jwsoMinuswm] = bode(H_jwsoMinuswm, logspace(1,6,200));
118 mag_H_jwsoMinuswm = squeeze(mag_H_jwsoMinuswm);
119 phase_H_jwsoMinuswm = squeeze(phase_H_jwsoMinuswm);
120
121 [mag_H_jwsoMinuswmConj phase_H_jwsoMinuswmConj] = bode(H_jwsoMinuswmConj, logspace
    (1,6,200));
122 mag_H_jwsoMinuswmConj = squeeze(mag_H_jwsoMinuswmConj);
123 phase_H_jwsoMinuswmConj = squeeze(phase_H_jwsoMinuswmConj);
124
125 Al_mag = -V_s1*J1_1.*mag_H_jwsoMinuswm;

```

```

126 AlConj_mag = -V_s1*J1_1.*mag_H_jwsoMinuswmConj;
127
128 %fundamental, sideband 2
129 alpha2 = 2;
130 J2_1 =besselj(alpha2,mag_beta);
131
132 %plus2wm
133 [mag_H_jwsoPlus2wm phase_H_jwsoPlus2wm] = bode(H_jwsoPlus2wm, logspace(1,6,200));
134 mag_H_jwsoPlus2wm = squeeze(mag_H_jwsoPlus2wm);
135 phase_H_jwsoPlus2wm = squeeze(phase_H_jwsoPlus2wm);
136
137 [mag_H_jwsoPlus2wmConj phase_H_jwsoPlus2wmConj] = bode(H_jwsoPlus2wmConj, logspace
    (1,6,200));
138 mag_H_jwsoPlus2wmConj = squeeze(mag_H_jwsoPlus2wmConj);
139 phase_H_jwsoPlus2wmConj = squeeze(phase_H_jwsoPlus2wmConj);
140
141 Au2_mag = V_s1*J2_1.*mag_H_jwsoPlus2wm;
142 Au2Conj_mag = V_s1*J2_1.*mag_H_jwsoPlus2wmConj;
143
144 %minus2wm
145 [mag_H_jwsoMinus2wm phase_H_jwsoMinus2wm] = bode(H_jwsoMinus2wm, logspace(1,6,200));
146 mag_H_jwsoMinus2wm = squeeze(mag_H_jwsoMinus2wm);
147 phase_H_jwsoMinus2wm = squeeze(phase_H_jwsoMinus2wm);
148
149 [mag_H_jwsoMinus2wmConj phase_H_jwsoMinus2wmConj] = bode(H_jwsoMinus2wmConj,
    logspace(1,6,200));
150 mag_H_jwsoMinus2wmConj = squeeze(mag_H_jwsoMinus2wmConj);
151 phase_H_jwsoMinus2wmConj = squeeze(phase_H_jwsoMinus2wmConj);
152
153 Al2_mag = V_s1*J2_1.*mag_H_jwsoMinus2wm;
154 Al2Conj_mag = V_s1*J2_1.*mag_H_jwsoMinus2wmConj;
155
156 %fundamental, sideband3
157 alpha3 = 3;
158 J3_1 =besselj(alpha3,mag_beta);
159
160 %plus3wm
161 [mag_H_jwsoPlus3wm phase_H_jwsoPlus3wm] = bode(H_jwsoPlus3wm, logspace(1,6,200));
162 mag_H_jwsoPlus3wm = squeeze(mag_H_jwsoPlus3wm);
163 phase_H_jwsoPlus3wm = squeeze(phase_H_jwsoPlus3wm);
164
165 [mag_H_jwsoPlus3wmConj phase_H_jwsoPlus3wmConj] = bode(H_jwsoPlus3wmConj, logspace
    (1,6,200));
166 mag_H_jwsoPlus3wmConj = squeeze(mag_H_jwsoPlus3wmConj);
167 phase_H_jwsoPlus3wmConj = squeeze(phase_H_jwsoPlus3wmConj);
168
169 Au3_mag = V_s1*J3_1.*mag_H_jwsoPlus3wm;

```

```

170 Au3Conj_mag = V_sl*J3_1.*mag_H_jwsoPlus3wmConj;
171
172 %minus3wm
173 [mag_H_jwsoMinus3wm phase_H_jwsoMinus3wm] = bode(H_jwsoMinus3wm, logspace(1,6,200));
174 mag_H_jwsoMinus3wm = squeeze(mag_H_jwsoMinus3wm);
175 phase_H_jwsoMinus3wm = squeeze(phase_H_jwsoMinus3wm);
176
177 [mag_H_jwsoMinus3wmConj phase_H_jwsoMinus3wmConj] = bode(H_jwsoMinus3wmConj,
    logspace(1,6,200));
178 mag_H_jwsoMinus3wmConj = squeeze(mag_H_jwsoMinus3wmConj);
179 phase_H_jwsoMinus3wmConj = squeeze(phase_H_jwsoMinus3wmConj);
180
181 Al3_mag = V_sl*J3_1.*mag_H_jwsoMinus3wm;
182 Al3Conj_mag = V_sl*J3_1.*mag_H_jwsoMinus3wmConj;
183
184 a1 = (Ao_mag.*AlConj_mag)+(Au_mag.*AoConj_mag)+(Al_mag.*Al2Conj_mag)+(Au2_mag.*
    AuConj_mag);
185 a2 = (Ao_mag.*Al2Conj_mag)+(Au_mag.*AlConj_mag)+(Al_mag.*Al3Conj_mag)+(Au2_mag.*
    AoConj_mag)+(Au3_mag.*AuConj_mag);
186 a3 = (Ao_mag.*Al3Conj_mag)+(Au_mag.*Al2Conj_mag)+(Au2_mag.*AlConj_mag)+(Au3_mag.*
    AoConj_mag);
187
188 fundamentalOutput = (sqrt((1/3)*(a1.^2+a2.^2+a3.^2)))/(Ao_mag);
189 fundamentalOutput = ((1/delta_w)*fundamentalOutput);
190
191 %%%%%%%%%%third harmonic
192
193 %with Rload
194 H_3jwso = tf([a*(3*i*w_so)^2],[b*(3*i*w_so)^3+c*(3*i*w_so)^2+d*(3*i*w_so)+e]);
195 H_3jwsoConj = tf([a*(-3*i*w_so)^2],[b*(-3*i*w_so)^3+c*(-3*i*w_so)^2+d*(-3*i*w_so)+e
    ]);
196
197 %with Rload
198 H_3jwsoPluswm = tf([a*a*6*i*w_so-a*9*w_so^2],[b*(b*9*i*w_so+c)*(-b*27*w_so^2+c*6*i*
    w_so+d)*(e-9*c*w_so^2-27*b*i*w_so^3+3*d*i*w_so)]);
199 H_3jwsoPluswmConj = tf([a*a*6*i*w_so-a*9*w_so^2],[-b*(-b*9*i*w_so+c)*(b*27*w_so^2+c
    *6*i*w_so-d)*(27*b*i*w_so^3-c*9*w_so^2-3*d*i*w_so+e)]);
200
201 %with Rload
202 H_3jwsoMinuswm = tf([a*-6*i*w_so*a-9*a*w_so^2],[-b*(b*9*i*w_so+c)*(b*27*w_so^2-c*6*
    i*w_so-d)*(e-27*b*j*w_so^3-9*c*w_so^2+3*d*i*w_so)]);
203 H_3jwsoMinuswmConj = tf([a*-6*i*w_so*a-9*a*w_so^2],[b*(-b*9*i*w_so+c)*(-b*27*w_so
    ^2-c*6*i*w_so+d)*(e-c*9*w_so^2+27*b*i*w_so^3-3*d*i*w_so)]);
204
205 %with Rload
206 H_3jwsoPlus2wm = tf([4*a-12*a*i*w_so-9*a*w_so^2],[8*b*(36*b*i*w_so+4*c)*(-b*54*
    w_so^2+12*i*c*w_so+2*d)*(e+3*d*i*w_so-27*b*i*w_so^3-9*c*w_so^2)]);

```



```

207 H_3jwsoPlus2wmConj = tf([4*a 12*a*i*w_so -9*a*w_so^2],[-8*b (-36*b*i*w_so+4*c) (b
      *54*w_so^2+12*i*w_so*c-2*d) (27*b*i*w_so^3-9*c*w_so^2-3*d*i*w_so+e) ]]);
208
209 %with Rload
210 H_3jwsoMinus2wm = tf([4*a -12*a*i*w_so -9*a*w_so^2],[-8*b (36*b*i*w_so+4*c) (54*b*
      w_so^2-12*c*i*w_so-2*d) (e+3*d*i*w_so-27*b*j*w_so^3-9*c*w_so^2) ]]);
211 H_3jwsoMinus2wmConj = tf([4*a -12*a*i*w_so -9*a*w_so^2],[8*b (-36*b*i*w_so+4*c)
      (-54*b*w_so^2-12*c*i*w_so+2*d) (e-3*i*d*w_so-9*c*w_so^2+27*b*i*w_so^3) ]]);
212
213 %wth Rload
214 H_3jwsoPlus3wm = tf([9*a 18*a*i*w_so -9*a*w_so^2],[27*b (81*b*i*w_so+9*c) (-81*b*
      w_so^2+18*c*i*w_so+3*d) (e+3*d*i*w_so-9*c*w_so^2-27*b*i*w_so^3) ]]);
215 H_3jwsoPlus3wmConj = tf([9*a 18*a*i*w_so -9*a*w_so^2],[-27*b (-81*b*i*w_so+9*c) (81*
      b*w_so^2+18*c*i*w_so-3*d) (e-3*i*d*w_so-9*c*w_so^2+27*b*i*w_so^3) ]]);
216
217 %with Rload
218 H_3jwsoMinus3wm = tf([9*a -18*a*i*w_so -9*a*w_so^2],[-27*b (81*b*i*w_so+9*c) (81*b*
      w_so^2-18*c*i*w_so-3*d) (e+3*d*i*w_so-9*c*w_so^2-27*b*i*w_so^3) ]]);
219 H_3jwsoMinus3wmConj = tf([9*a -18*a*i*w_so -9*a*w_so^2],[27*b (-81*b*i*w_so+9*c)
      (-81*b*w_so^2-18*c*i*w_so+3*d) (e-3*d*i*w_so-9*c*w_so^2+27*b*i*w_so^3) ]]);
220
221 %third Harmonic, sideband 0
222 alpha0_3 = 0;
223 J0_3 = besselj(alpha0_3,mag_beta);
224
225 [mag_H_3jwso phase_H_3jwso] = bode(H_3jwso, logspace(1,6,200));
226 mag_H_3jwso = squeeze(mag_H_3jwso);
227 phase_H_3jwso = squeeze(phase_H_3jwso);
228
229 [mag_H_3jwsoConj phase_H_3jwsoConj] = bode(H_3jwsoConj, logspace(1,6,200));
230 mag_H_3jwsoConj = squeeze(mag_H_3jwsoConj);
231 phase_H_3jwsoConj = squeeze(phase_H_3jwsoConj);
232
233 Bo_mag = V_s3*J0_3.*mag_H_3jwso;
234 BoConj_mag = V_s3*J0_3.*mag_H_3jwsoConj;
235
236 %thirdHarmonic, sideband1
237 alpha1_3 = 1;
238 J1_3 = besselj(alpha1_3,mag_beta);
239
240 %3 plus
241 [mag_H_3jwsoPluswm phase_H_3jwsoPluswm] = bode(H_3jwsoPluswm, logspace(1,6,200));
242 mag_H_3jwsoPluswm = squeeze(mag_H_3jwsoPluswm);
243 phase_H_3jwsoPluswm = squeeze(phase_H_3jwsoPluswm);
244
245 [mag_H_3jwsoPluswmConj phase_H_3jwsoPluswmConj] = bode(H_3jwsoPluswmConj, logspace
      (1,6,200));

```

```

246 mag_H_3jwsoPluswmConj = squeeze(mag_H_3jwsoPluswmConj);
247 phase_H_3jwsoPluswmConj = squeeze(phase_H_3jwsoPluswmConj);
248
249 Bu_mag = V_s3*J1_3.*mag_H_3jwsoPluswm;
250 BuConj_mag = V_s3*J1_3.*mag_H_3jwsoPluswmConj;
251
252 %3 minus
253 [mag_H_3jwsoMinuswm phase_H_3jwsoMinuswm] = bode(H_3jwsoMinuswm, logspace(1,6,200));
254 mag_H_3jwsoMinuswm = squeeze(mag_H_3jwsoMinuswm);
255 phase_H_3jwsoMinuswm = squeeze(phase_H_3jwsoMinuswm);
256
257 [mag_H_3jwsoMinuswmConj phase_H_3jwsoMinuswmConj] = bode(H_3jwsoMinuswmConj,
    logspace(1,6,200));
258 mag_H_3jwsoMinuswmConj = squeeze(mag_H_3jwsoMinuswmConj);
259 phase_H_3jwsoMinuswmConj = squeeze(phase_H_3jwsoMinuswmConj);
260
261 Bl_mag = -V_s3*J1_3.*mag_H_3jwsoMinuswm;
262 BlConj_mag = -V_s3*J1_3.*mag_H_3jwsoMinuswmConj;
263
264 %thirdHarmonic, sideband2
265 alpha2_3 = 2;
266 J2_3 = besselj(alpha2_3,mag_beta);
267
268 %3 plus2
269 [mag_H_3jwsoPlus2wm phase_H_3jwsoPlus2wm] = bode(H_3jwsoPlus2wm, logspace(1,6,200));
270 mag_H_3jwsoPlus2wm = squeeze(mag_H_3jwsoPlus2wm);
271 phase_H_3jwsoPlus2wm = squeeze(phase_H_3jwsoPlus2wm);
272
273 [mag_H_3jwsoPlus2wmConj phase_H_3jwsoPlus2wmConj] = bode(H_3jwsoPlus2wmConj,
    logspace(1,6,200));
274 mag_H_3jwsoPlus2wmConj = squeeze(mag_H_3jwsoPlus2wmConj);
275 phase_H_3jwsoPlus2wmConj = squeeze(phase_H_3jwsoPlus2wmConj);
276
277 Bu2_mag = V_s3*J2_3.*mag_H_3jwsoPlus2wm;
278 Bu2Conj_mag = V_s3*J2_3.*mag_H_3jwsoPlus2wmConj;
279
280 %3 minus2
281 [mag_H_3jwsoMinus2wm phase_H_3jwsoMinus2wm] = bode(H_3jwsoMinus2wm, logspace
    (1,6,200));
282 mag_H_3jwsoMinus2wm = squeeze(mag_H_3jwsoMinus2wm);
283 phase_H_3jwsoMinus2wm = squeeze(phase_H_3jwsoMinus2wm);
284
285 [mag_H_3jwsoMinus2wmConj phase_H_3jwsoMinus2wmConj] = bode(H_3jwsoMinus2wmConj,
    logspace(1,6,200));
286 mag_H_3jwsoMinus2wmConj = squeeze(mag_H_3jwsoMinus2wmConj);
287 phase_H_3jwsoMinus2wmConj = squeeze(phase_H_3jwsoMinus2wmConj);
288

```

```

289 Bl2_mag = -V_s3*J2_3.*mag_H_3jwsoMinus2wm;
290 Bl2Conj_mag = -V_s3*J2_3.*mag_H_3jwsoMinus2wmConj;
291
292 %thridHarmonic, sideband3
293 alpha3_3 = 3;
294 J3_3 =besselj(alpha3_3,mag_beta);
295
296 %3 plus3
297 [mag_H_3jwsoPlus3wm phase_H_3jwsoPlus3wm] = bode(H_3jwsoPlus3wm, logspace(1,6,200));
298 mag_H_3jwsoPlus3wm = squeeze(mag_H_3jwsoPlus3wm);
299 phase_H_3jwsoPlus3wm = squeeze(phase_H_3jwsoPlus3wm);
300
301 [mag_H_3jwsoPlus3wmConj phase_H_3jwsoPlus3wmConj] = bode(H_3jwsoPlus3wmConj,
    logspace(1,6,200));
302 mag_H_3jwsoPlus3wmConj = squeeze(mag_H_3jwsoPlus3wmConj);
303 phase_H_3jwsoPlus3wmConj = squeeze(phase_H_3jwsoPlus3wmConj);
304
305 Bu3_mag = V_s3*J3_3.*mag_H_3jwsoPlus3wm;
306 Bu3Conj_mag = V_s3*J3_3.*mag_H_3jwsoPlus3wmConj;
307
308 %3 minus3
309 [mag_H_3jwsoMinus3wm phase_H_3jwsoMinus3wm] = bode(H_3jwsoMinus3wm, logspace
    (1,6,200));
310 mag_H_3jwsoMinus3wm = squeeze(mag_H_3jwsoMinus3wm);
311 phase_H_3jwsoMinus3wm = squeeze(phase_H_3jwsoMinus3wm);
312
313 [mag_H_3jwsoMinus3wmConj phase_H_3jwsoMinus3wmConj] = bode(H_3jwsoMinus3wmConj,
    logspace(1,6,200));
314 mag_H_3jwsoMinus3wmConj = squeeze(mag_H_3jwsoMinus3wmConj);
315 phase_H_3jwsoMinus3wmConj = squeeze(phase_H_3jwsoMinus3wmConj);
316
317 Bl3_mag = -V_s3*J3_3.*mag_H_3jwsoMinus3wm;
318 Bl3Conj_mag = -V_s3*J3_3.*mag_H_3jwsoMinus3wmConj;
319
320 b1 = (Bo_mag.*BlConj_mag)+(Bu_mag.*BoConj_mag)+(Bl_mag.*Bl2Conj_mag)+(Bu2_mag.*
    BuConj_mag);
321 b2 = (Bo_mag.*Bl2Conj_mag)+(Bu_mag.*BlConj_mag)+(Bl_mag.*Bl3Conj_mag)+(Bu2_mag.*
    BoConj_mag)+(Bu3_mag.*BuConj_mag);
322 b3 = (Bo_mag.*Bl3Conj_mag)+(Bu_mag.*Bl2Conj_mag)+(Bu2_mag.*BlConj_mag)+(Bu3_mag.*
    BoConj_mag);
323
324 thirdHarmonicOutput = (sqrt((1/3)*(b1.^2+b2.^2+b3.^2)))/(Bo_mag);
325 thirdHarmonicOutput = ((1/delta_w)*thirdHarmonicOutput);
326
327 %%%%%%%%%fifth harmonic
328
329 %with Rload

```

```

330 H_5jwso = tf([a*(5*i*w_so)^2],[b*(5*i*w_so)^3+c*(5*i*w_so)^2+d*(5*i*w_so)+e]);
331 H_5jwsoConj = tf([a*(-5*i*w_so)^2],[b*(-5*i*w_so)^3+c*(-5*i*w_so)^2+d*(-5*i*w_so)+e
    ]);
332
333 %with Rload
334 H_5jwsoPluswm = tf([a a*10*i*w_so -a*25*w_so^2],[b (b*15*i*w_so+c) (-b*75*w_so^2+c
    *10*i*w_so+d) (e-25*c*w_so^2-125*b*i*w_so^3+5*d*i*w_so)]);
335 H_5jwsoPluswmConj = tf([a a*10*i*w_so -a*25*w_so^2],[-b (-b*15*i*w_so+c) (b*75*w_so
    ^2+c*10*i*w_so-d) (125*b*i*w_so^3-c*25*w_so^2-5*d*i*w_so+e)]);
336
337 %with Rload
338 H_5jwsoMinuswm = tf([a -10*i*w_so*a -25*a*w_so^2],[-b (b*15*i*w_so+c) (b*75*w_so^2-c
    *10*i*w_so-d) (e-125*b*j*w_so^3-25*c*w_so^2+5*d*i*w_so)]);
339 H_5jwsoMinuswmConj = tf([a -10*i*w_so*a -25*a*w_so^2],[b (-b*15*i*w_so+c) (-b*75*
    w_so^2-c*10*i*w_so+d) (e-c*25*w_so^2+125*b*i*w_so^3-5*d*i*w_so)]);
340
341 %with Rload
342 H_5jwsoPlus2wm = tf([4*a 20*a*i*w_so -25*a*w_so^2],[8*b (60*b*i*w_so+4*c) (-b*150*
    w_so^2+20*i*c*w_so+2*d) (e+5*d*i*w_so-125*b*i*w_so^3-25*c*w_so^2)]);
343 H_5jwsoPlus2wmConj = tf([4*a 20*a*i*w_so -25*a*w_so^2],[-8*b (-60*b*i*w_so+4*c) (b
    *150*w_so^2+20*i*w_so*c-2*d) (125*b*i*w_so^3-25*c*w_so^2-5*d*i*w_so+e)]);
344
345 %with Rload
346 H_5jwsoMinus2wm = tf([4*a -20*a*i*w_so -25*a*w_so^2],[-8*b (60*b*i*w_so+4*c) (150*b*
    w_so^2-20*c*i*w_so-2*d) (e+5*d*i*w_so-125*b*j*w_so^3-25*c*w_so^2)]);
347 H_5jwsoMinus2wmConj = tf([4*a -20*a*i*w_so -25*a*w_so^2],[8*b (-60*b*i*w_so+4*c)
    (-150*b*w_so^2-20*c*i*w_so+2*d) (e-5*i*d*w_so-25*c*w_so^2+125*b*i*w_so^3)]);
348
349 %with Rload
350 H_5jwsoPlus3wm = tf([9*a 30*a*i*w_so -25*a*w_so^2],[27*b (135*b*i*w_so+9*c) (-225*b*
    w_so^2+30*c*i*w_so+3*d) (e+5*d*i*w_so-25*c*w_so^2-125*b*i*w_so^3)]);
351 H_5jwsoPlus3wmConj = tf([9*a 30*a*i*w_so -25*a*w_so^2],[-27*b (-135*b*i*w_so+9*c)
    (225*b*w_so^2+30*c*i*w_so-3*d) (e-5*i*d*w_so-25*c*w_so^2+125*b*i*w_so^3)]);
352
353 %with Rload
354 H_5jwsoMinus3wm = tf([9*a -30*a*i*w_so -25*a*w_so^2],[-27*b (135*b*i*w_so+9*c) (225*
    b*w_so^2-30*c*i*w_so-3*d) (e+5*d*i*w_so-25*c*w_so^2-125*b*i*w_so^3)]);
355 H_5jwsoMinus3wmConj = tf([9*a -30*a*i*w_so -25*a*w_so^2],[27*b (-135*b*i*w_so+9*c)
    (-225*b*w_so^2-30*c*i*w_so+3*d) (e-5*d*i*w_so-25*c*w_so^2+125*b*i*w_so^3)]);
356
357 %fifthHarmonic , sideband0
358 alpha0_5 = 0;
359 J0_5 = besselj(alpha0_5,mag_beta);
360
361 [mag_H_5jwso phase_H_5jwso] = bode(H_5jwso, logspace(1,6,200));
362 mag_H_5jwso = squeeze(mag_H_5jwso);
363 phase_H_5jwso = squeeze(phase_H_5jwso);

```

```

364
365 [mag_H_5jwsoConj phase_H_5jwsoConj] = bode(H_5jwsoConj, logspace(1,6,200));
366 mag_H_5jwsoConj = squeeze(mag_H_5jwsoConj);
367 phase_H_5jwsoConj = squeeze(phase_H_5jwsoConj);
368
369 Co_mag = V_s5*J0_5.*mag_H_5jwso;
370 CoConj_mag = V_s5*J0_5.*mag_H_5jwsoConj;
371
372 %fifthHarmonic, sideband1
373 alpha1_5 = 1;
374 J1_5 =besselj(alpha1_5,mag_beta);
375
376 %5 plus
377 [mag_H_5jwsoPluswm phase_H_5jwsoPluswm] = bode(H_5jwsoPluswm, logspace(1,6,200));
378 mag_H_5jwsoPluswm = squeeze(mag_H_5jwsoPluswm);
379 phase_H_5jwsoPluswm = squeeze(phase_H_5jwsoPluswm);
380
381 [mag_H_5jwsoPluswmConj phase_H_5jwsoPluswmConj] = bode(H_5jwsoPluswmConj, logspace
    (1,6,200));
382 mag_H_5jwsoPluswmConj = squeeze(mag_H_5jwsoPluswmConj);
383 phase_H_5jwsoPluswmConj = squeeze(phase_H_5jwsoPluswmConj);
384
385 Cu_mag = V_s5*J1_5.*mag_H_5jwsoPluswm;
386 CuConj_mag = V_s5*J1_5.*mag_H_5jwsoPluswmConj;
387
388 %5 minus
389 [mag_H_5jwsoMinuswm phase_H_5jwsoMinuswm] = bode(H_5jwsoMinuswm, logspace(1,6,200));
390 mag_H_5jwsoMinuswm = squeeze(mag_H_5jwsoMinuswm);
391 phase_H_5jwsoMinuswm = squeeze(phase_H_5jwsoMinuswm);
392
393 [mag_H_5jwsoMinuswmConj phase_H_5jwsoMinuswmConj] = bode(H_5jwsoMinuswmConj,
    logspace(1,6,200));
394 mag_H_5jwsoMinuswmConj = squeeze(mag_H_5jwsoMinuswmConj);
395 phase_H_5jwsoMinuswmConj = squeeze(phase_H_5jwsoMinuswmConj);
396
397 Cl_mag = -V_s5*J1_5.*mag_H_5jwsoMinuswm;
398 ClConj_mag = -V_s5*J1_5.*mag_H_5jwsoMinuswmConj;
399
400 %fifthHarmonic, sideband2
401 alpha2_5 = 2;
402 J2_5 =besselj(alpha2_5,mag_beta);
403
404 %5 plus2
405 [mag_H_5jwsoPlus2wm phase_H_5jwsoPlus2wm] = bode(H_5jwsoPlus2wm, logspace(1,6,200));
406 mag_H_5jwsoPlus2wm = squeeze(mag_H_5jwsoPlus2wm);
407 phase_H_5jwsoPlus2wm = squeeze(phase_H_5jwsoPlus2wm);
408

```

```

409 [mag_H_5jwsoPlus2wmConj phase_H_5jwsoPlus2wmConj] = bode(H_5jwsoPlus2wmConj,
    logspace(1,6,200));
410 mag_H_5jwsoPlus2wmConj = squeeze(mag_H_5jwsoPlus2wmConj);
411 phase_H_5jwsoPlus2wmConj = squeeze(phase_H_5jwsoPlus2wmConj);
412
413 Cu2_mag = V_s5*J2_5.*mag_H_5jwsoPlus2wm;
414 Cu2Conj_mag = V_s5*J2_5.*mag_H_5jwsoPlus2wmConj;
415
416 %5 minus2
417 [mag_H_5jwsoMinus2wm phase_H_5jwsoMinus2wm] = bode(H_5jwsoMinus2wm, logspace
    (1,6,200));
418 mag_H_5jwsoMinus2wm = squeeze(mag_H_5jwsoMinus2wm);
419 phase_H_5jwsoMinus2wm = squeeze(phase_H_5jwsoMinus2wm);
420
421 [mag_H_5jwsoMinus2wmConj phase_H_5jwsoMinus2wmConj] = bode(H_5jwsoMinus2wmConj,
    logspace(1,6,200));
422 mag_H_5jwsoMinus2wmConj = squeeze(mag_H_5jwsoMinus2wmConj);
423 phase_H_5jwsoMinus2wmConj = squeeze(phase_H_5jwsoMinus2wmConj);
424
425 Cl2_mag = -V_s5*J2_5.*mag_H_5jwsoMinus2wm;
426 Cl2Conj_mag = -V_s5*J2_5.*mag_H_5jwsoMinus2wmConj;
427
428 %fifthHarmonic , sideband3
429 alpha3_5 = 3;
430 J3_5 =besselj(alpha3_5,mag_beta);
431
432 %5 plus3
433 [mag_H_5jwsoPlus3wm phase_H_5jwsoPlus3wm] = bode(H_5jwsoPlus3wm, logspace(1,6,200));
434 mag_H_5jwsoPlus3wm = squeeze(mag_H_5jwsoPlus3wm);
435 phase_H_5jwsoPlus3wm = squeeze(phase_H_5jwsoPlus3wm);
436
437 [mag_H_5jwsoPlus3wmConj phase_H_5jwsoPlus3wmConj] = bode(H_5jwsoPlus3wmConj,
    logspace(1,6,200));
438 mag_H_5jwsoPlus3wmConj = squeeze(mag_H_5jwsoPlus3wmConj);
439 phase_H_5jwsoPlus3wmConj = squeeze(phase_H_5jwsoPlus3wmConj);
440
441 Cu3_mag = V_s5*J3_5.*mag_H_5jwsoPlus3wm;
442 Cu3Conj_mag = V_s5*J3_5.*mag_H_5jwsoPlus3wmConj;
443
444 %5 minus3
445 [mag_H_5jwsoMinus3wm phase_H_5jwsoMinus3wm] = bode(H_5jwsoMinus3wm, logspace
    (1,6,200));
446 mag_H_5jwsoMinus3wm = squeeze(mag_H_5jwsoMinus3wm);
447 phase_H_5jwsoMinus3wm = squeeze(phase_H_5jwsoMinus3wm);
448
449 [mag_H_5jwsoMinus3wmConj phase_H_5jwsoMinus3wmConj] = bode(H_5jwsoMinus3wmConj,
    logspace(1,6,200));

```

```

450 mag_H_5jwsoMinus3wmConj = squeeze(mag_H_5jwsoMinus3wmConj);
451 phase_H_5jwsoMinus3wmConj = squeeze(phase_H_5jwsoMinus3wmConj);
452
453 Cl3_mag = -V_s5*J3_5.*mag_H_5jwsoMinus3wm;
454 Cl3Conj_mag = -V_s5*J3_5.*mag_H_5jwsoMinus3wmConj;
455
456 c1 = (Co_mag.*ClConj_mag)+(Cu_mag.*CoConj_mag)+(Cl_mag.*Cl2Conj_mag)+(Cu2_mag.*
      CuConj_mag);
457 c2 = (Co_mag.*Cl2Conj_mag)+(Cu_mag.*ClConj_mag)+(Cl_mag.*Cl3Conj_mag)+(Cu2_mag.*
      CoConj_mag)+(Cu3_mag.*CuConj_mag);
458 c3 = (Co_mag.*Cl3Conj_mag)+(Cu_mag.*Cl2Conj_mag)+(Cu2_mag.*ClConj_mag)+(Cu3_mag.*
      CoConj_mag);
459
460 fifthHarmonicOutput = (sqrt((1/3)*(c1.^2+c2.^2+c3.^2)))/(Co_mag);
461 fifthHarmonicOutput = ((1/delta_w)*fifthHarmonicOutput);
462
463
464 finalOutput = (fundamentalOutput+thirdHarmonicOutput+fifthHarmonicOutput)*2*pi*
      Tratio.*(mag_ESRzero).^1.*(mag_RHPzero).^2.*(mag_ZOHpole).^3;
465
466 % plots
467 plota = semilogx(wout/(2*pi),20*log10(fundamentalOutput),'b');hold on,
468 plotb = semilogx(wout/(2*pi),20*log10(thirdHarmonicOutput),'g');hold on,
469 plotc = semilogx(wout/(2*pi),20*log10(fifthHarmonicOutput),'r');hold on,
470 hold on, plotd= semilogx(wout/(2*pi),20*log10(finalOutput),'k')
471 hold on, bode([0],[1],[2*pi*600,2*pi*1e4])
472 hold on
473 legend([plota,plotb,plotc,plotd])

```